2012-07-06

Development of Motion Artifact Rejection Algorithms for Ambulatory Heart Rate and Arterial Oxygen Measurement By A Wearable Pulse Oximeter

Kunal Marwah

Department of Biomedical Engineering

Development of Motion Artifact Rejection Algorithms for Ambulatory Heart Rate and Arterial Oxygen Measurement By A Wearable Pulse Oximeter

A Thesis

Submitted to the Faculty of

WORCESTER POLYTECHNIC INSTITUTE

In partial fulfillment of the requirements for the

Degree of Master of Science

By

Kunal Marwah

Professor Yitzhak Mendelson, Primary Advisor
Department of Biomedical Engineering

Professor Ki Chon, Committee Member
Department of Biomedical Engineering

Professor Domhnull Granquist Fraser, Committee Member
Department of Biomedical Engineering

ACKNOWLEDGEMENTS

I would like to express my sincere gratitude to Prof Yitzhak Mendelson for giving me the opportunity to work on this project and for his valuable guidance, help, support and patience over the past year.

I am also very thankful to Prof Ki Chon and Prof Fraser for agreeing to be a part of my thesis committee and for their valuable comments and suggestions that have tremendously helped in improving the quality of research.

I am also very grateful to Nandakumar Selveraj for integrating me into the MNA project, Chris Scully for his constant support and valuable inputs that have greatly helped in improving my skills.

I would like to thank Jinsoek Lee and John Favreau for taking the time to help me with all my Matlab difficulties. Alan Humphrey and Duy Dao for helping me compile and format my thesis report

Finally, I would also like to thank my mother for her constant support and belief in my abilities that have helped me reach this far.

ABSTRACT

Over the past decade, there has been an increasing interest in the real-time monitoring of ambulatory vital signs such as heart rate (HR) and arterial blood oxygen saturation (SpO_2) using wearable medical sensors during field operations. These measurements can convey valuable information regarding the state of health and allow first responders and front-line medics to better monitor and prioritize medical intervention of military combatants, firefighters, miners and mountaineers in case of medical emergencies. However, the primary challenge encountered when using these sensors in a non-clinical environment has been the presence of persistent motion artifacts (MA) embedded in the acquired physiological signal. These artifacts are caused by the random displacement of the sensor from the skin and lead to erroneous output readings.

Several signal processing techniques, such as time and frequency domain segmentation, signal reconstruction techniques and adaptive noise cancellation (ANC), have been previously developed in an offline environment to address MA in photoplethysmography (PPG) with varying degrees of success. However, the performance of these algorithms in a spasmodic noise environment usually associated with basic day to day ambulatory activities has still not been fully investigated. Therefore, the focus of this research has been to develop novel MA algorithms to combat the effects of these artifacts.

The specific aim of this thesis was to design two novel motion artifact (MA) algorithms using a combination of higher order statistical tools namely Kurtosis (K) for classifying 10 s PPG data segments, as either ‘clean’ or ‘corrupt’ and then extracting the aforementioned vital parameters. To overcome the effects of MA, the first algorithm (termed ‘MNA’) processes these ‘corrupt’ PPG data segments by identifying abnormal amplitudes changes. The second algorithm (termed ‘MNAC’), filters these ‘corrupt’ data segments using a 16^{th} order normalized least mean square (NLMS) ANC filter and then extracts HR and SpO_2.

Table of Content

List of Figures

List of Tables

Glossary of Abbreviations

ACC	Accelerometer
ANC	Adaptive Noise Cancellation
BPM	Beats per minute
CSA	Current Sensor Algorithm
HSA	Heart Rate and SpO2 algorithms
HR	Heart Rate
HSA	Heart rate and SpO_2 algorithms
K	Kurtosis
LMS	Least Mean Square
SE	Shannon Entropy
MA	Motion Artifact(s)
MNA	Motion/Noise Artifact Algorithm
MNAC	MNA Algorithm using adaptive noise cancellation
NLMS	Normalized Least Mean Square
SpO_2	Arterial Oxygen Saturation Level

1. Introduction

Over the past decade, there has been an increasing interest in real time (R/T) monitoring ambulatory vital signs such as heart rate (HR) and arterial oxygen saturation (SpO_2) using wearable medical sensors during field operations. These measurements are pertinent as they convey valuable information regarding the state of health of military combatants, firefighters, miners and mountaineers and allow first responders and front-line medics to better monitor and prioritize medical intervention in case of medical emergencies, thereby extending more effective care to casualties with most urgent needs [1]. This increasing interest has resulted in the tremendous market growth of such sensors with sales expected to reach approximately $170 million dollars by 2017 with an estimated annual growth rate of 10% [2].

Pulse oximeters are devices that are widely used due to their inexpensive and rugged nature as well as their ease of access to a measuring site. They have the ability to accurately measure the subject's HR with comparable accuracy to a three channel ECG [3], [4] as well as SpO_2 with comparable accuracy to an invasive blood-gas monitor [5]. Oximeters are commonly placed on the finger, earlobe or forehead and are used for continuous data acquisition.

A similar wearable pulse oximeter as shown in Figure 1.1 has been designed by Advanced Body Sensing (ABS) [6]. This sensor can be mounted on a person's forehead and has the ability to wirelessly monitor their HR, SpO_2 and respiratory rate (RR). It also provides information regarding body posture and movement with the help of an embedded accelerometer (ACC) and wirelessly transmits all information to a nearby laptop computer with the help of the USB based transceiver.

Figure 1.1. ABS forehead mounted sensor.

However, the primary challenge encountered when using these devices in a nonclinical environment has been the presence of persistent motion artifacts (MA) embedded in the acquired physiological signal. These artifacts are caused by the random displacement of the sensor from the skin which leads to the degradation in signal quality [7]. This causes large and abnormal variations in the output values that can lead to frequent false alarms, thereby reducing the diagnostic confidence in the instrument's overall ability which can prove to be detrimental, especially in a high risk environment.

In the past, several signal processing techniques such as time and frequency domain segmentation, signal reconstruction techniques and adaptive noise cancellation (ANC) have been developed to address this problem with varying degrees of success. However, the performance of these algorithms in a noisy environment associated with basic day to day ambulatory activities has still not been fully investigated. Therefore, the focus of our research has been to develop novel MA algorithms capable of improving the accuracy of HR and SpO_2.

The specific aim of this thesis was to develop two novel MA rejection algorithms using a combination of higher order statistical tools, Kurtosis (K) and Shannon Entropy (SE), for classifying a R/T photoplethysmogram (PPG) signal as either ‘clean’ or ‘corrupt’ and then using these segments to extract the aforementioned vital parameters.

The final goal of this work would be to conduct a preliminary field study with test subjects in a spurious noise environment to analyze the performance of both algorithms. The potential use of these algorithms would be to help minimize some of the challenges associated with MA and allow wireless monitoring of vital parameters during physical activities such as walking, climbing, jogging and running. Moreover, these algorithms would also have the ability to be implemented on existing pulse oximeters without the need for any hardware changes.

2. Background

Commercially developed in 1972 with the help of principles described by Takuo Aoyagi, pulse oximetry is the first method that provided physicians the ability to noninvasively measure a person's arterial oxygen saturation (SaO_2) [8]. By the mid 1980's, it was adopted as a standard of care in both the operating room as well as critical care units for continuously monitoring oxygen saturation. Thereby assisting anesthesiologists prevent fatal brain injuries caused by hypoxemia in unconscious and comatose patients incapable of regulating their own oxygen supply [8]. This section covers some of the basic principles involved in the functionality of a pulse oximeter.

2.1. Photoplethysmography (PPG)

A pulse oximeter makes use of a PPG signal to extract vital information from a subject by illuminating a portion of the skin and measuring either the reflected or transmitted light with the help of a photodetector component. It is defined as a noninvasive technique to detect blood volume changes in the microvascular bed of tissue [9]. There are mainly two types of pulse oximeters:

- Transmission Mode
- Reflectance Mode

As shown in Figure 2.1, in the transmission mode, the light emitting diodes (LED) and the photodetector components which converts incident light into equivalent voltages are mounted on the opposite side of the measuring probe. Most clinically used oximeters are transmission type where the photodetector component collects the light transmitted through the finger, earlobe or even the toes of the patient.

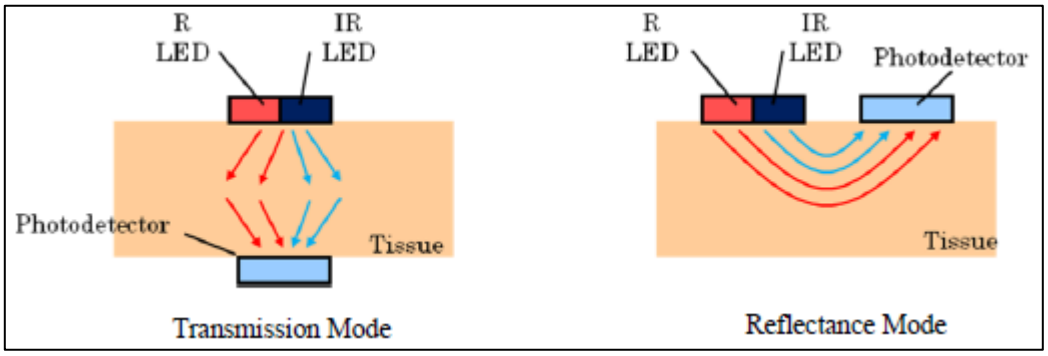

Figure 2.1. Types of Pulse Oximetry [10].

In the reflectance mode, the photodetectors are on the same side as the LEDs. This type of pulse oximeters are typically mounted on the forehead and have proved to be a better alternative for field applications due their ability to provide measuring sites that are unobstructive in performing daily activities. Moreover, PPG signals acquired using reflectance based forehead sensors have shown to have a better signal to noise ratio (SNR) in the presence of MA [11], [12]. Therefore, for the purpose of our work we choose to use this type of sensor.

The primary application of pulse oximetry has been to noninvasively determine blood oxygen saturation levels. The principle of these measurements is based on Beer-Lambert law, which states that the concentration of an unknown solute can be determined by light absorption. The governing principle

as illustrated in Figure 2.2, has been the difference in optical absorbance exhibited between oxyhemoglobin (HbO_2) and reduced hemoglobin (Hb) for different light wavelengths. HbO_2 absorbs less red (R) light (λ =660nm) compared to Hb for fully oxygenated blood, whereas HbO_2 absorbs more infrared (IR) light (λ =940) compared to Hb [13]. The use of two wavelengths to determine the oxygen saturation is termed as SpO_2. The Gaussian distribution shown at 660nm and 940nm indicates the LEDs power distribution of the R and IR wavelengths.

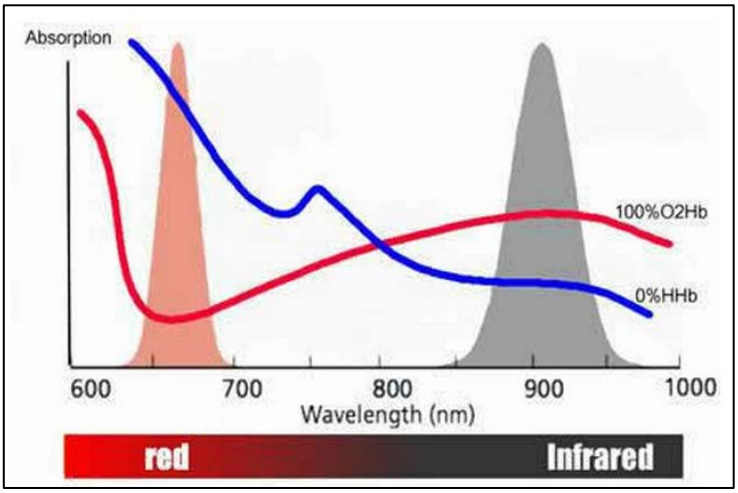

Figure 2.2. Optical absorbance spectra of blood for SpO_2 measurements [14].

On acquiring either the reflected or transmitted light, the PPG signal is separated into two signal components, the pulsatile AC component and a slow varying DC component as illustrated in Figure 2.3. The AC component is governed by the principle that the amount of light absorbed is inversely proportional to the pumping action of the heart. During peak systolic phase the attenuation of light increases due to the rapid arterial blood flow whereas the attenuation decreases as the blood flows out of the arteries during peak diastolic phase [15]. This results in a pulsatile wave which is commonly referred to as the AC component of the PPG signal. This pulsatile wave is superimposed on a large quasi DC component attributed to absorption of light by the tissue, bone, non-pulsatile arterial and venous blood [9], [16].

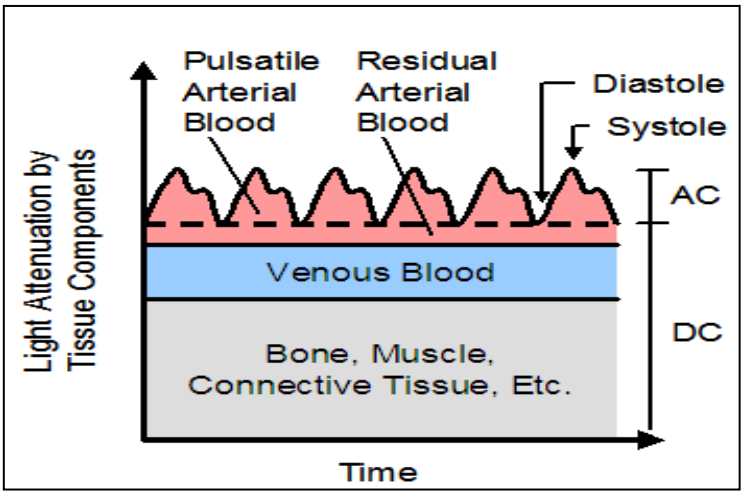

Figure 2.3 Light attenuation through skin and tissue [17].

2.1.1. Measurement of Arterial Oxygen Saturation

The principle of SpO_2 measurement is based on computing the AC and DC components for the R and IR light and then using the following equation:

$$SpO_2 = A - B\frac{(AC/DC)_R}{(AC/DC)_{IR}} \tag{2.1}$$

where A and B are equal to 110 and 25, respectively [18].

Commercially, A and B are derived using an empirically derived calibration curve as shown in Figure 2.4 by comparing the pulse oximeter readings to values obtained from in vitro measurements using a pool of healthy volunteers [13]. As the optical properties of blood are almost identical for different individuals, these values don't need to be individually calibrated [13].

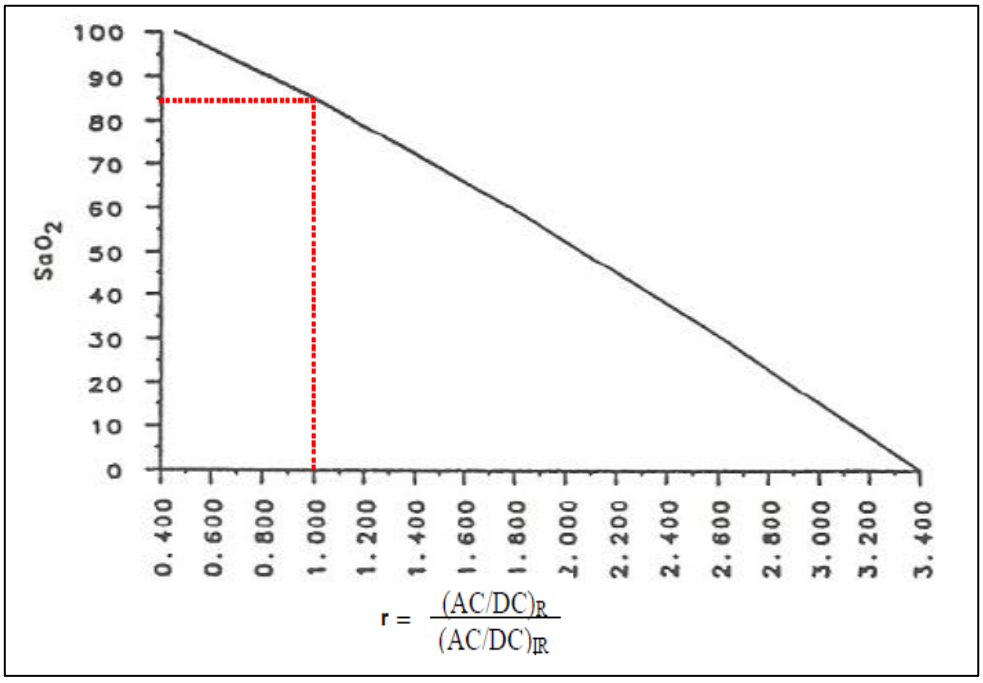

Figure 2.4. Empirical relationship between SaO_2 and r [13].

2.1.2. SpO_2 Ranges

For healthy patients, the range of SpO_2 between 95%-99% is considered to be normal [19]. These levels help identify hypoxemia, which is defined as the deficiency of oxygen in arterial blood and usually indicates a need of oxygen supplementation [20]. In the clinical environment the onset of hypoxemia is considered when the SpO_2 level falls below 90% especially for post anesthesia care units. An alarm in triggered at 85% to prevent severe brain injuries [21]. Other clinical applications of SpO_2 monitoring include diagnosing sleep apneas [22].

2.2. PPG Signal Processing

In terms of signal processing, a raw PPG signal can be filtered into its corresponding AC and DC by using conventional filtering techniques as depicted in Figure 2.5. In our research, to extract the AC component we make use of a 4^{th} order bandpass infinite impulse response (IIR) Butterworth filter with a passband frequency range of 0.5-3Hz. On the other hand, to extract the DC component we use a 4^{th} order lowpass Butterworth filter with cut off frequency of 0.05 Hz, a passband ripple of 3dB and a stopband attenuation of 40dB. The sampling frequency of the PPG signal obtained from the ABS sensor is fixed at 80 Hz.

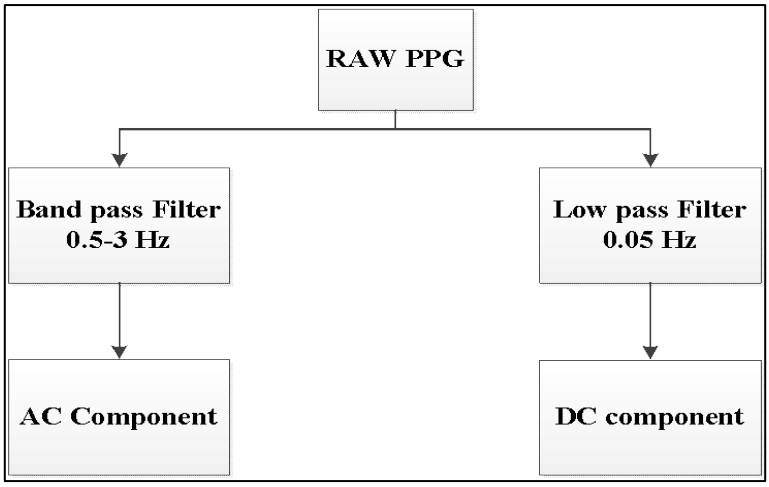

Figure 2.5. Basic filtering flowchart of a PPG signal.

An example of the above signal processing technique can be iterated with the help of Figure 2.6 where Fig. 2.6.A. shows the time varying AC component obtained from the band pass filter and whereas Fig 2.6.B. depicts the time invariant DC component. The peaks in the AC component correspond to the peak diastole whereas the troughs coincide with peak systolic phase during the rhythmic contraction of the heart.

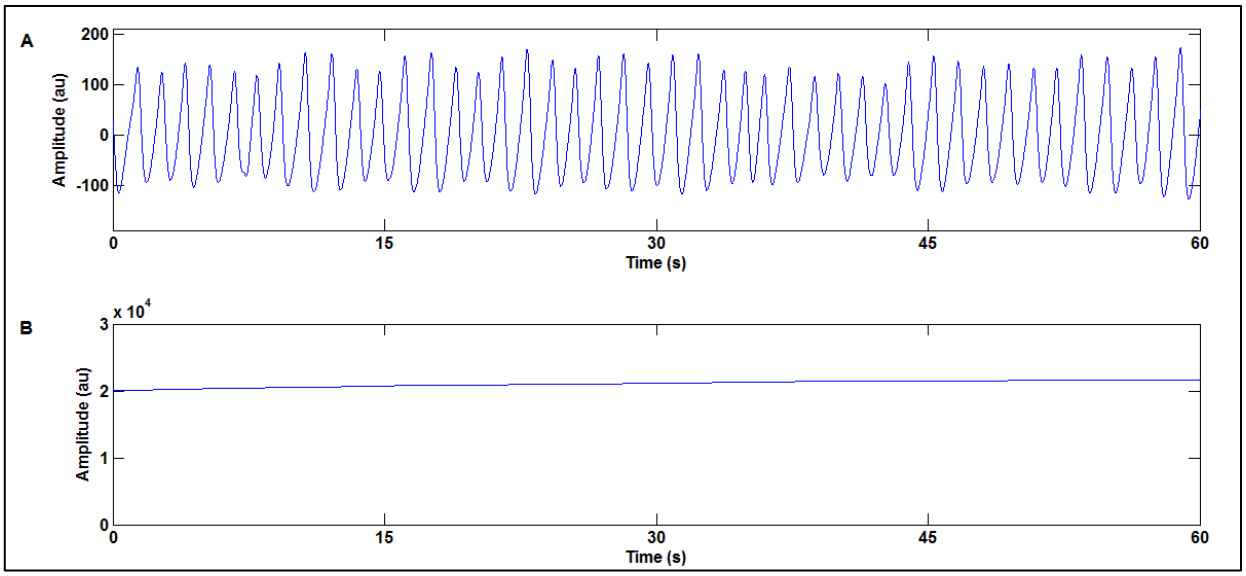

Figure 2.6. AC (A) and DC (B) components of a typical PPG signal.

2.2.1. Vital Parameter Estimation

- **HR**

  The instantaneous HR value (IHR) can be extracted using the AC component of the PPG. As described earlier, the AC component is based on the rhythmic contraction of the heart. Therefore, IHR can be determined by computing the time interval between two successive peaks/troughs in the AC component and then using the following equation:

$$\boxed{HR = \frac{60}{T}} \qquad (2.3)$$

  where T (sec) is the time interval between successive peaks. On dividing 60 by this time interval, we obtain IHR values in beats per minute (BPM).

  In terms of computing HR from the ABS sensor, we make use of a customized peak detection algorithm on the IR-AC PPG and then use Equation 2.3. This process is illustrated in Figure 2.7 where the peak detection algorithm is used on the AC component of a filtered IR-PPG to obtain the IHR. In order to avoid outliers we input the IHR values through a 10 point moving average filter to obtain the final HR value.

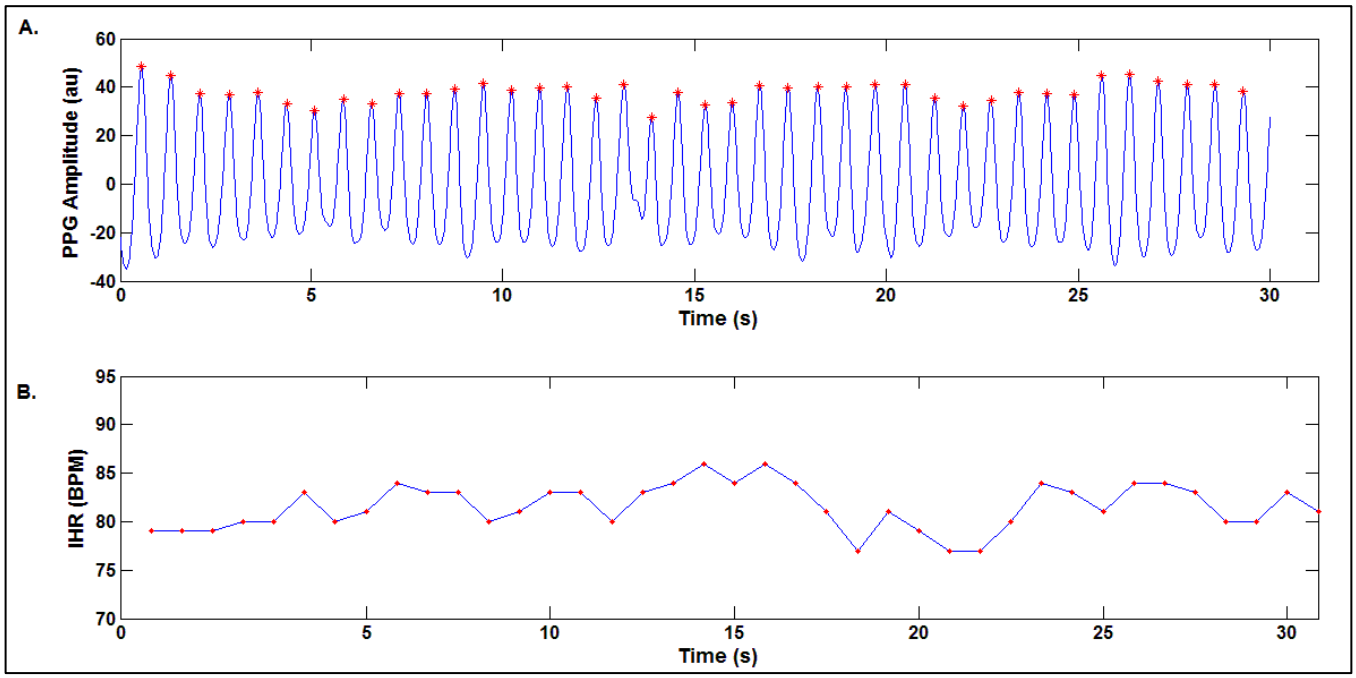

Figure 2.7. A typical IR-AC(A) along with its corresponding IHR(B) values. '*' in (A) indicate detected peaks, whereas 'o' in (B) indicate HR values in BPM.

- **SpO_2**

  In terms of SpO_2 computation, the ABS sensor identifies the peaks of the R and IR peaks from the AC component. It then computes a point by point r value using the corresponding DC component as shown in Figure 2.8 (a). Finally, all the computed SpO_2 are averaged using a moving average filter; which further enhances its computational efficiency [23] . Alternately, SpO_2 computation can also be done by taking a single step change per heart beat and then computing SpO_2 as shown in Figure 2.8 (b).

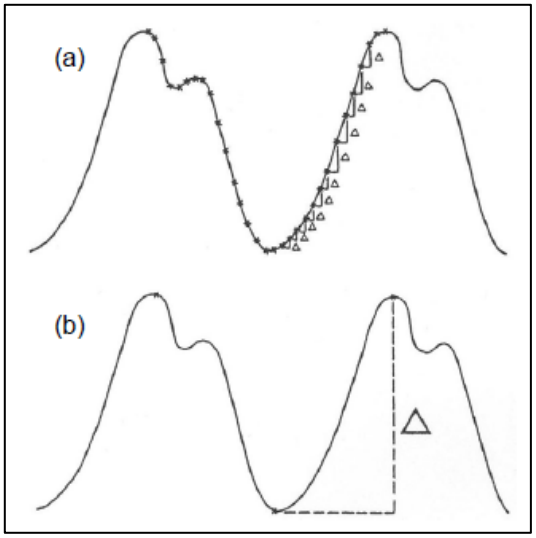

Figure 2.8: Using a combination of fixed steps (a) and moving averages versus (b) a single step change to compute SpO_2 [13].

2.3. Limitations of Pulse Oximetry

Despite obvious benefits, some limitations of pulse oximetry include:

- An inaccurately low oxygen saturation estimation for individuals with a dark pigmented skin with constant output values in the range of 70-80% [24].
- False low readings due to the exposure of the photodetector to ambient light [20].
- Venous pulsation caused by the arterial blood being shunted into the veins, result in false low SpO_2 readings [25]
- Abnormally high readings during certain ailments such as anemia and carboxyhemoglobin [26] .

Other limitations of pulse oximetry include its inability to obtain accurate results in the presence of MA which can be caused by limb movements. MA leads to lower perfusion index (PI) (defined as the ratio of AC and DC component of R or IR) and poor signal to noise ratios causing inaccurate output readings [1], [13] , [26], [27]. The effects of MA and its implications vital parameter readings are discussed in the next chapter.

3. Motion Artifacts

3.1. Effects of Motion Artifacts

The effect of MA is a complex issue with multiple viewpoints. The obvious effect is the deterioration in the quality of the recorded PPG signal.

Early research conducted on the cause of these artifacts by Langton and Hanning examined the correlation between exerted forces caused by movement of the subject which spasmodically dislodged the sensor from the skin [27]. This work concluded that MA affected both the IR and R causing abnormally high r (Figure 2.4) values (closer to 1) which consequently affected SpO_2 readings, causing false oxygen saturation levels closer to 85%. Further investigation has also theorized that subject motion can also lead to the movement of the venous blood as well as other non-pulsatile components [28]. This causes the AC component of the PPG signal to be composed of more than just arterial blood, leading to false desaturation levels of around 50 % [29]. An example of a clean IR-AC PPG signal is shown in Figure 3.1 (A) where the IR-AC signal conveys information regarding the rhythmic contraction of the heart whereas Figure 3.1 (B) shows a walking IR-AC PPG, corrupted by motion artifacts.

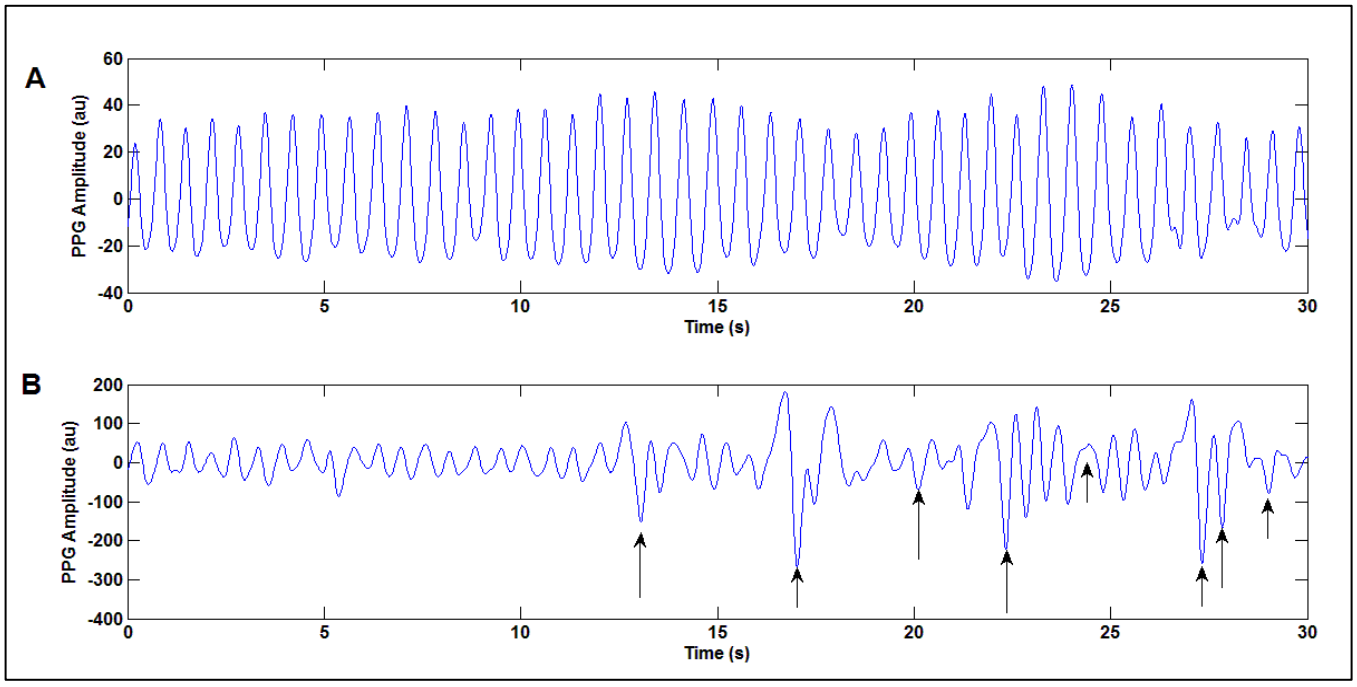

Figure 3.1. Typical (A) Clean (B) Noisy PPG. Arrow indicates false peaks caused due to motion.

In terms of the frequency domain, Figure 3.2 shows the Fast Fourier Transforms (FFT) of the clean and noisy signals shown in Figure 3.1. Ideally, the FFT should consist of one dominant frequency which symbolizes the instantaneous HR of that segment. However, we observe that MA induces additional frequency components in the 0.5-3Hz range, which could have an adverse effect on these readings leading to inaccurate results.

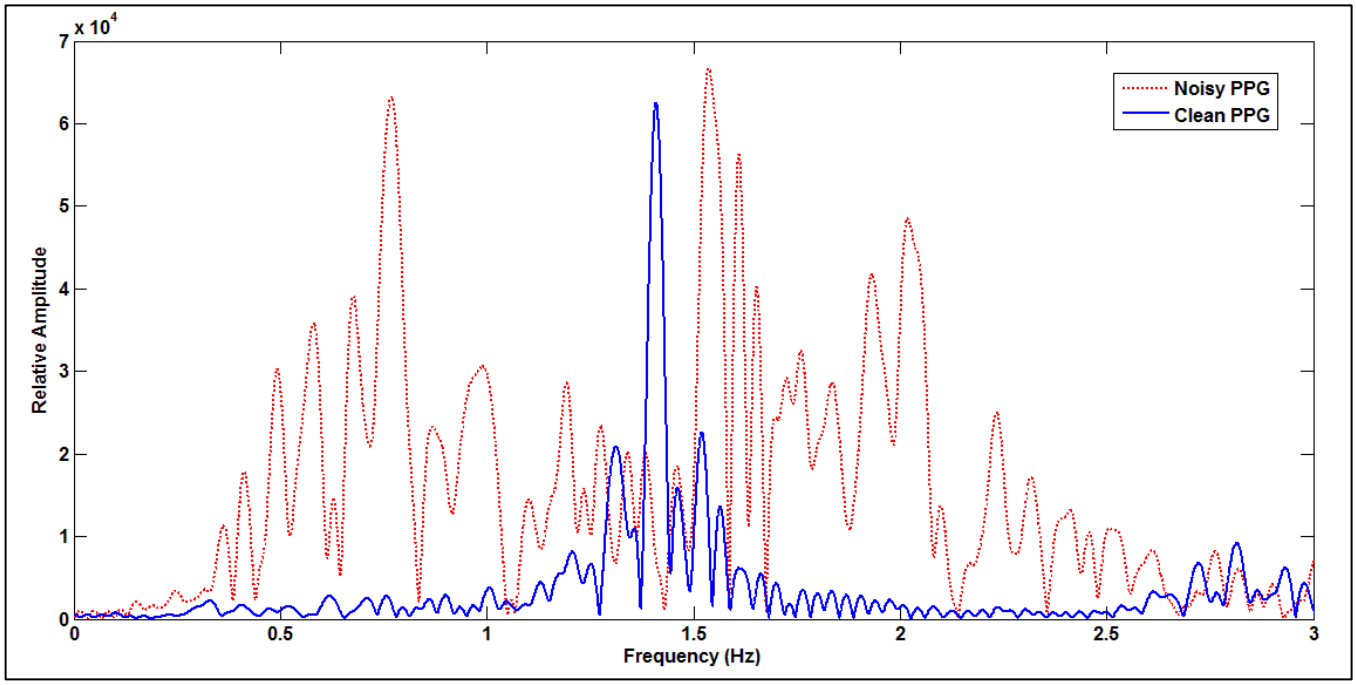

Figure 3.2. Frequency spectrum of a clean and corrupt PPG.

Specifically in terms of aberrant HRs, Figure 3.3 shows corrupted IR-AC segment from Figure 3.1(B) processed by the ABS sensor's HR algorithm to obtain IHR values. Due to the presence of false peaks we observe an unusual variance in the output readings during walking which is abnormal for a healthy person. Such stark changes in HR readings could induce false alarms during field and clinical operations and raise concerns relating to the proper functionality of the device.

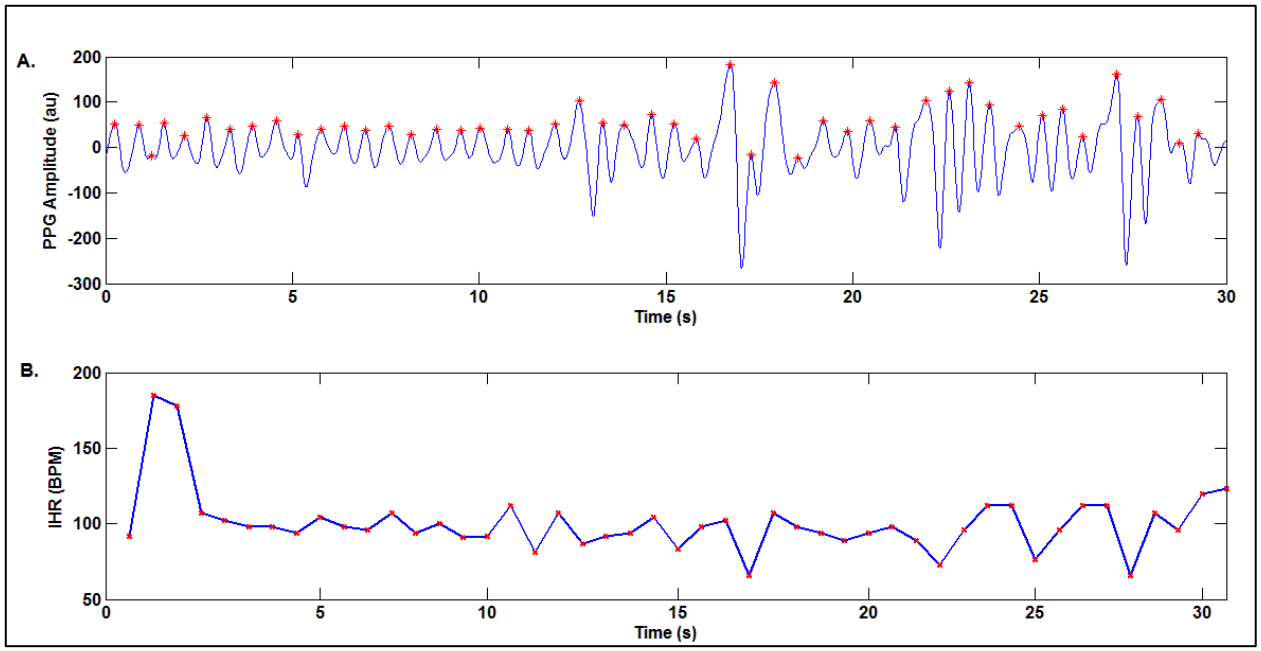

Figure 3.3. Walking PPG corrupted by MA (A) and its estimated IHR (B). Here '*' in (A) indicates detected peaks.

Similarly, Figure 3.4 shows the corresponding SpO_2 values estimated from the corrupted IR (shown in Figure 3.1(B)) and its corresponding R PPG's. It is quite apparent that MA adversely affects the accuracy of these readings as such stark changes would indicate a chronic illness which is not true in this case.

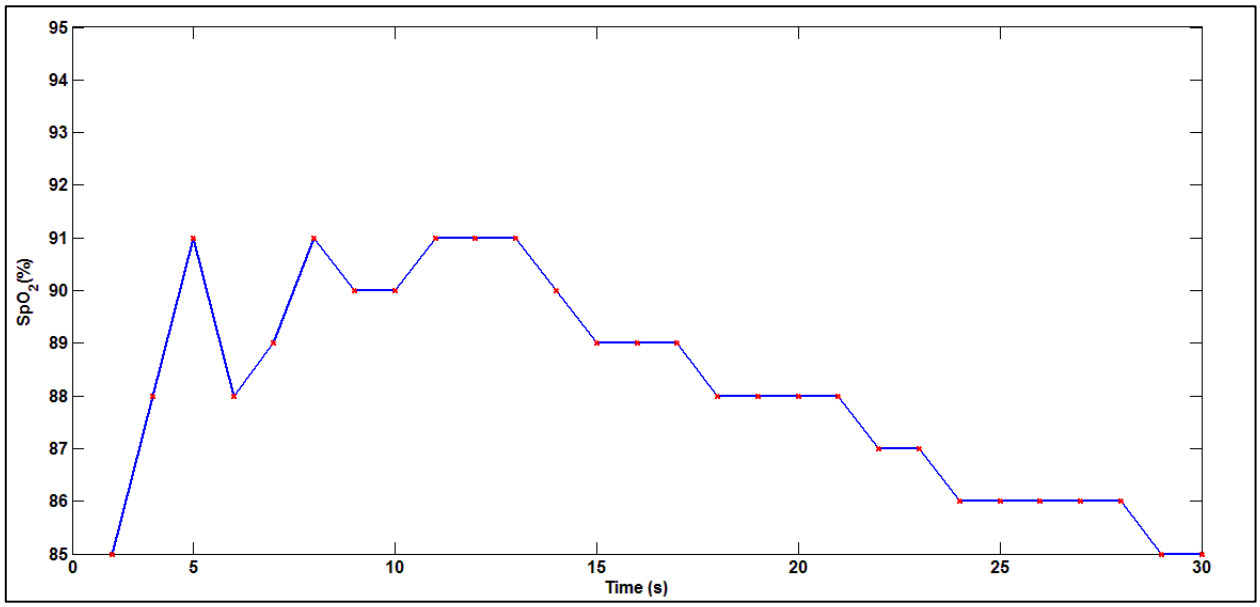

Figure 3.4. Corrupt SpO_2 reading derived from a noisy PPG.

In the past, large clinical scale studies done in the intensive care units have shown that over 70% of the alarms were caused by MA [30] [31]. This has a potential disadvantage of inducing a 'cry wolf syndrome' leading to a lower urgency response time of critically ill patients due to persistent false alarms.

We next investigated the effects of MA in terms of obtaining HR and SpO_2 values obtained from a wearable commercial pulse oximeter during certain physical activities which induced a variety of MA. This study was conducted in order to assess the performance of existing mobile oximeters in terms of tackling MA in an outdoor environment.

3.1.1. Effects of MA on a wearable pulse oximeter

For this study, we used a CMS 50F wristwatch pulse oximeter distributed by Southeastern Medical [32] as shown in Figure 3.5. As a preliminary experiment, we placed this sensor on the left index finger of a volunteer and monitored the changes in HR and SpO_2 during rest, walking and stair climbing. In terms of a reference standard, we attached a 3 lead ECG Holter monitor to the volunteer's chest to get reference HR values and a Masimo® bench top pulse oximeter on left ring finger to get reference SpO_2 values.

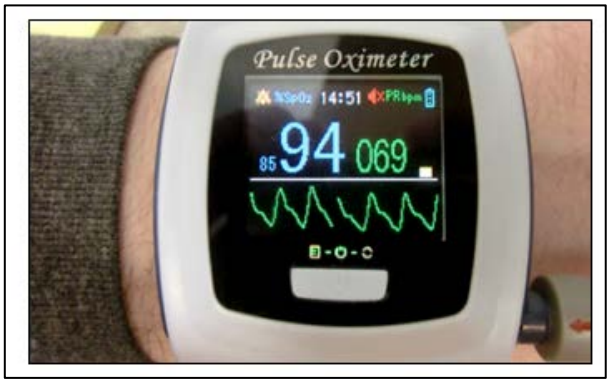

Figure 3.5. CMS 50F watch pulse oximeter.

Figure 3.6 shows the HR progression during the course of the experiment. Despite the volunteer making conscious efforts to avoid any rapid hand movements, the watch HR was unable to keep up with the ECG derived HR. Similar results were also seen when these tests were done on different subjects.

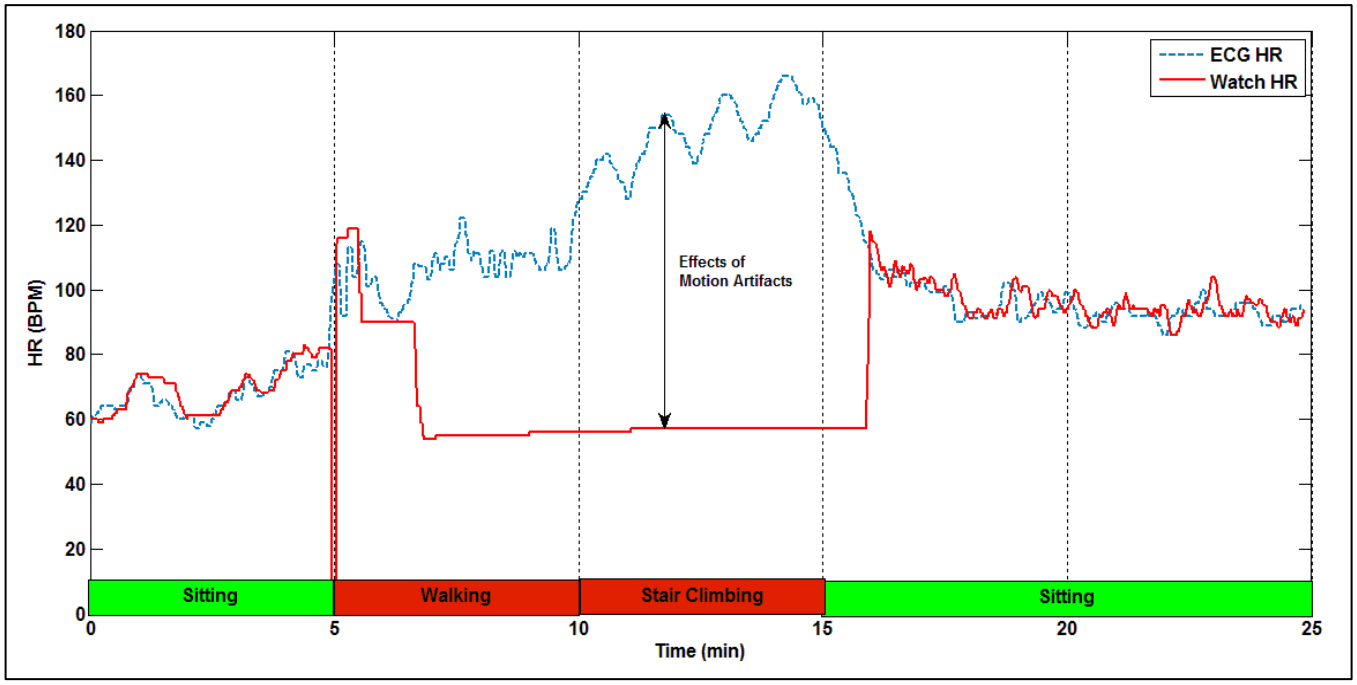

Figure 3.6. HR readings obtained from the CMS 50F pulse oximter during the outdoor experiment.

The following conclusions were drawn from these experiments:

- The CMS 50F was unable to counter motion artifacts as a result it did not update the HR readings frequently.
- The output HR readings stagnated during exercise which can be a cause of worry as it produces misleading results that can be prejudicial especially in a high risk environment.

Similarly, the sensor's SpO_2 readings results for the same experiment as shown in Figure 3.7. These reading were compared to a Masimo SET pulse oximeter which in the past has shown to be most effective in tackling MA in critical care units compared to other commercially available products [33].

Ideally, the SpO_2 values for a healthy person should remain unchanged in a resting state. Though physiological change of upto 2-3% have been observed during strenuous exercise to keep up with the increasing oxygen demand but should still remain above 92% [34]. In this experiment as no strenuous exercise was performed, therefore the stark changes in oxygen saturation can only be as a result of MA [35].

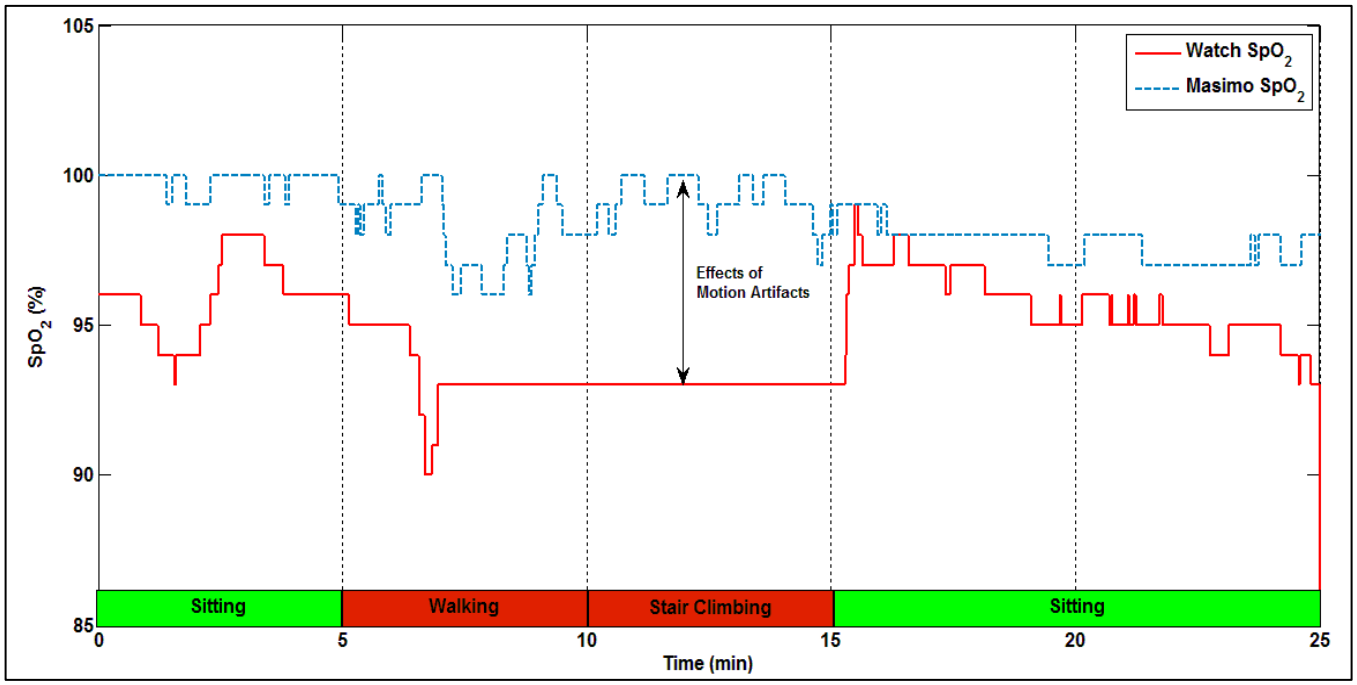

Figure 3.7. SpO_2 reading obtained from the CMS 50F pulse oximter for the outdoor experiment.

3.2. Overcoming Motion Artifacts

In the past, several MA algorithms based on a variety of signal processing techniques have been developed to minimize the effects of MA and extract useful information from the corrupted PPG signals. These include moving average filters to detect sporadic changes in signal amplitudes [36], independent component analysis (ICA) [37], singular value decomposition (SVD) [38] and wavelet transforms [39]. However, the effectiveness of moving average filters has shown to be reduced when in the presence of large or abrupt signal amplitudes changes caused by motion [36]. Similarly, limitations of wavelet transforms include a phase-shift in the reconstructed signal [40] as well the use of a static signal threshold to reconstruct the clean PPG signal which may not be viable for different subjects [41]. Lastly ICA, which works on the principle of statistical independence between arterial pulsation and MA has shown to be incorrect [42].

Another widely researched technique to counter the effects of MA has been the use of ANC filters [43], [44]. These filters are advantageous as they require no prior knowledge about the characteristics of the signal and the noise [45]. Their adaptive output is solely dependent on an independent reference signal which is typically obtained from an accelerometer (ACC) embedded in the device and is assumed to be correlated to the artifacts present in the physiological signal. Some of the R/T applications of ANC specific to PPG signal processing includes, implementation of a least mean square (LMS) adaptive filter [46], normalized least mean square (NLMS) filter [47] and adaptive step size least mean square (AS-LMS) filter [48]. Similar filters including LMS, NLMS, Time-Varying LMS (TV-LMS) and

Recursive Least Square (RLS) have also been previously studied in our lab [10]. In addition to ANC, higher order statistical methods that forego the need of complex signal processing techniques in the system have also shown to be useful in detecting artifacts in ECG [49] and PPG signals [50], [51]. However, the quantitative performance analysis of these measures on different individuals and in comparison with existing commercial devices still needs to be investigated. Therefore, there is a need to develop an R/T approach to accurately detect and compensate for MA under practical scenarios for a variety of physical activities. Hence, the focus of this thesis was to investigate the viability of some of these statistical parameters in conjunction with existing vital parameter extraction algorithms.

4. Adaptive Noise Cancellation (ANC)

ANC filtering differs from conventional filters due to its ability to constantly update filter coefficients depending on the nature of the noise present in the input signal. A block-diagram of the basic implementation workflow of ANC filters is shown in Figure 4.1.

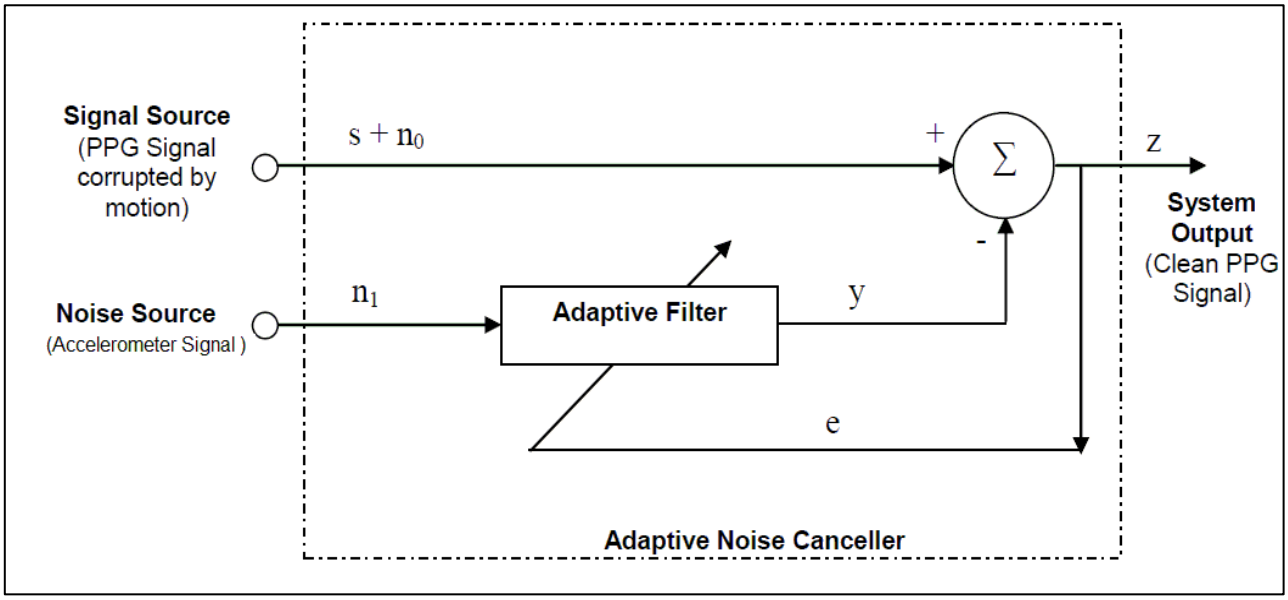

Figure 4.1. ANC basic block diagram [52].

Specific to the ABS sensor, ANC is implemented by using the tri-axis (X+ Y + Z) output signal obtained from the ACC as the independent noise source (n_1). This signal is assumed to be correlated with the noise present in the PPG segment, specifically to MA. On subtracting the noise segment from the signal source, a relatively clean PPG signal (z) should be obtained. This output is again fed back to the filter as an error signal (e=z) and used for updating the filter coefficients for the next iteration. The goal of the ANC filter is to minimize this error coefficient by using different mathematical approaches such as least mean squares (LMS) or recursive least squares (RLS).

4.1. Signal Processing of Accelerometer Outputs

The output from the ACC is firstly preprocessed using the same signal processing techniques used on a PPG signal as described in Figure 2.5. The three axis of the ACC component i.e. X, Y, Z are initially combined and then filtered into their respective AC and DC components. The AC component is characteristic to the subject's movement and is used as the input noise source (n_1) for ANC implementation whereas the DC component conveys information regarding body posture/orientation.

To get a sense of different ACC outputs, we plotted simultaneous IR-AC and ACC-AC plots during rest and walking. Figure 4.2 shows a 1 min recording of an IR-AC component superimposed on the ACC output obtained from the ABS sensor. As there is no significant movement by the subject, the ACC output wanders around the origin and output an steady state value while we obtain a recognizably clean PPG signal.

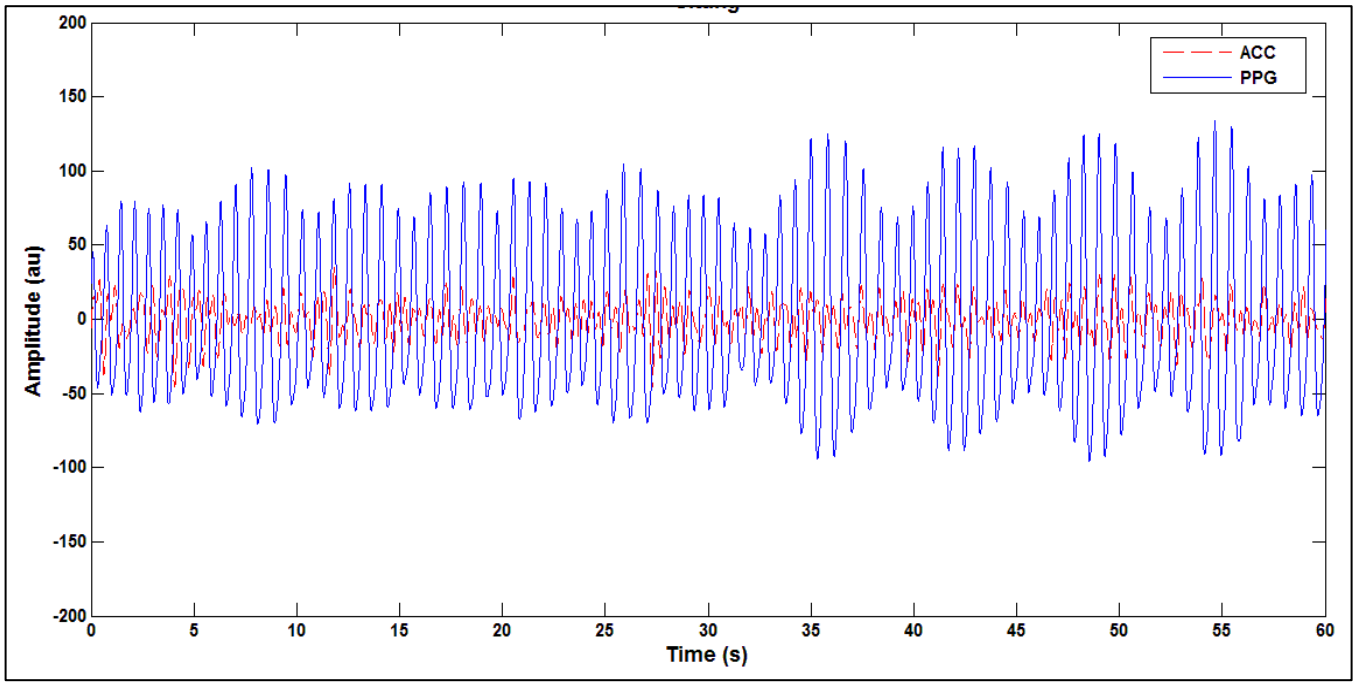

Figure 4.2. AC component of resting PPG vs. corresponding ACC-AC output.

Figure 4.3 shows a recording done during a walking experiment where certain regions of the PPG signal are corrupted by motion artifacts. Here, the ACC-AC component also has a much higher signal amplitude and the y-axis of the figure has a much wider range due to continous body movement which leads to continous high signal amplitude obtained from the ACC.

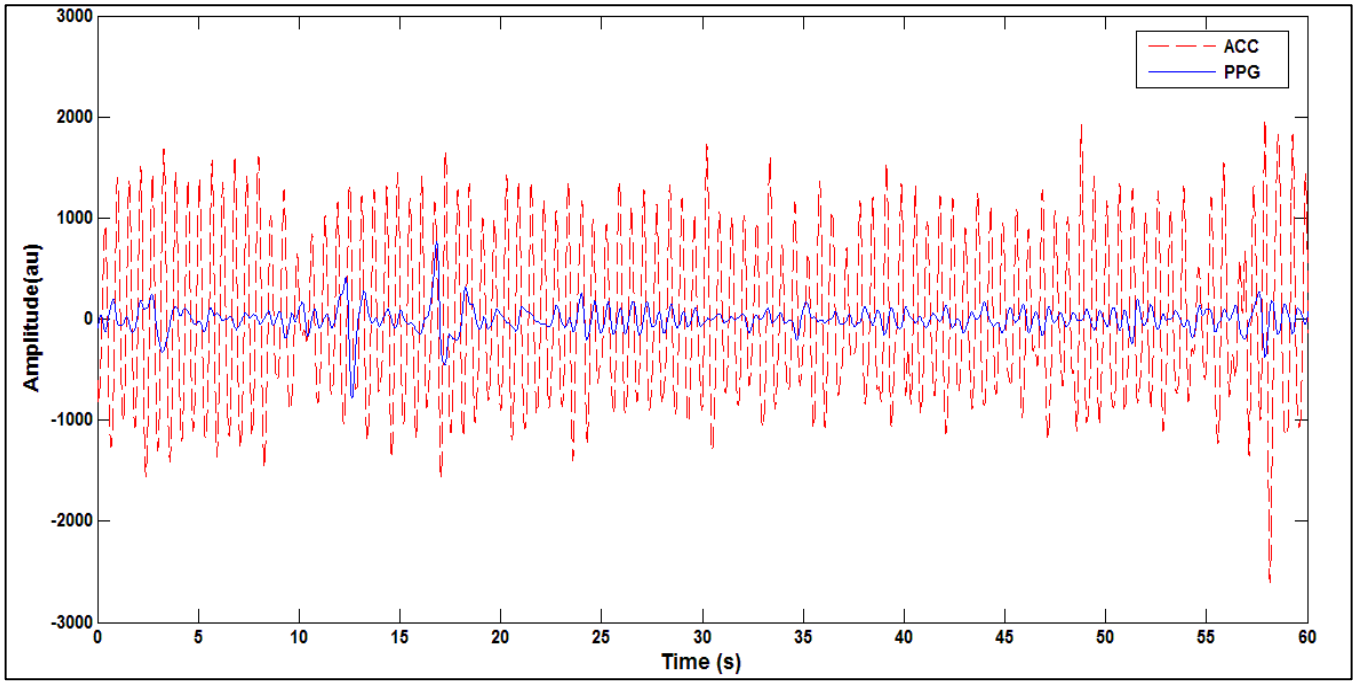

Figure 4.3. AC component of walking PPG vs. corresponding ACC-AC outputs.

4.2. Frequency Analysis of Accelerometer Outputs

In terms of the frequency analysis, the FFT of the corrupted PPG segment (as shown in Figure 3.1) along with its corresponding ACC output are shown in Figure 4.4. The peaks in the raw IR signal indicate MA whereas the peaks in the ACC signal indicate body movement. During ANC implementation, the objective of the adaptive filters is to remove the overlapping ACC and PPG frequency components, thereby minimizing the effects of motion artifact and outputting a relatively clean signal.

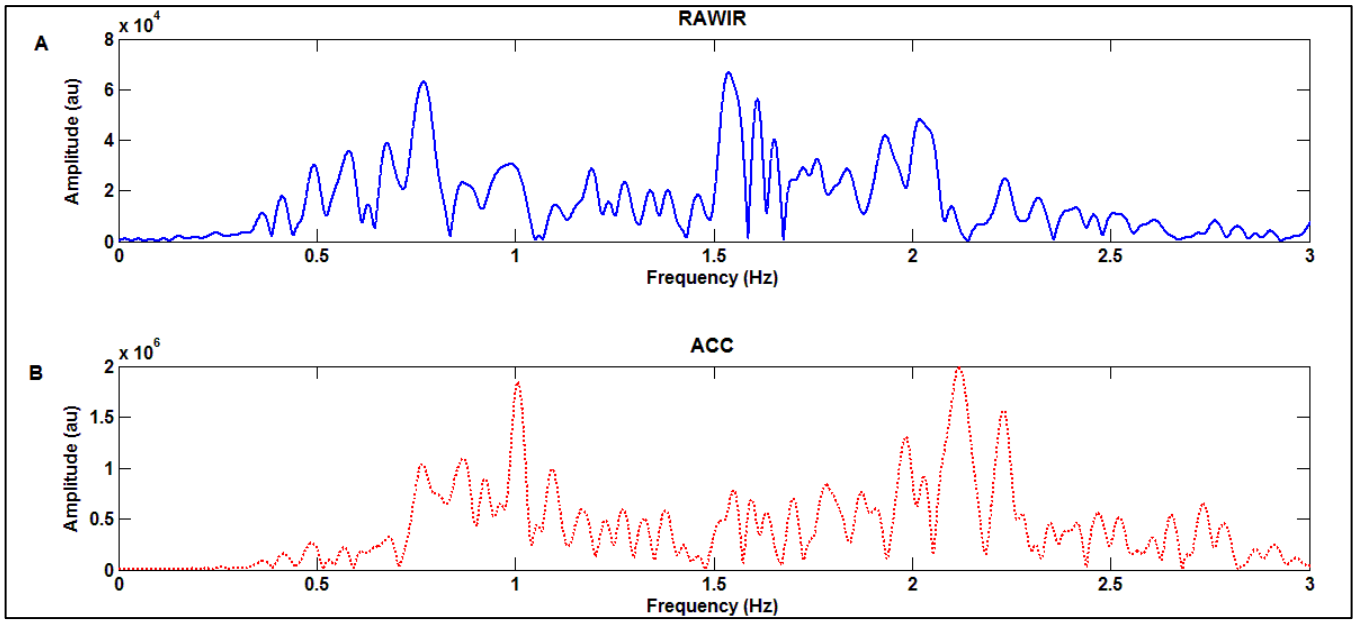

Figure 4.4. Frequency spectrum of walking raw IR PPG (A) and the corresponding ACC signal (B).

A typical example of the ANC filtering is shown in Figure 4.5. This method potentially prevents false peak detection and helps to avoid abnormal IHR variability.

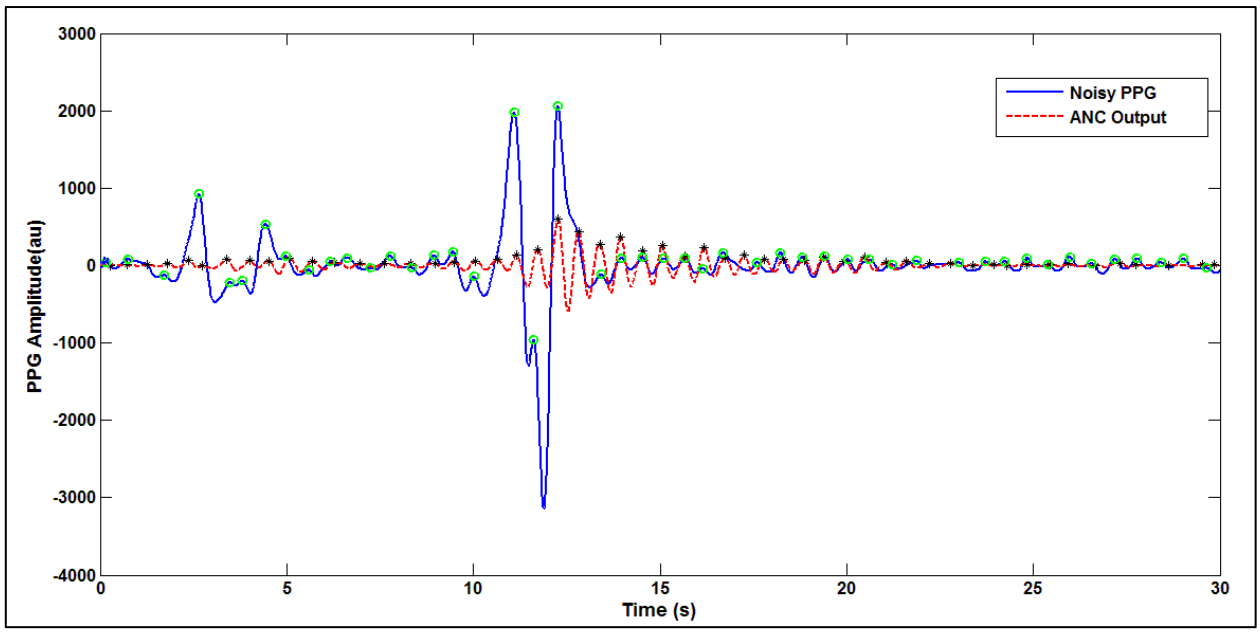

Figure 4.5. Example of a corrupted and ANC filtered PPG signal. '*' indicate the peaks detected in the corrupted PPG, whereas 'o' indicate peaks in the filtered PPG.

Now, we investigate the potential use of higher order statistics as a means of triggering ANC during R/T implementation. For this thesis, we would only be working with the NLMS filter previously designed by [10] to study the feasibility of this concept.

4.3. Normalized Least Mean Square Algorithm (NLMS)

The LMS algorithm is based on the stochastic implementation of the steepest descent algorithm. Starting with arbitrary filter weights, the algorithm converges in order to minimize the total output power, thus causing the system output to be a best least square estimate of the desired signal [10].

The performance of the LMS algorithm is highly dependent on the selected filter order and convergence factor (μ) [53]. A smaller μ leads to a slower convergence rate with a better accuracy [54]. However, the main drawback of the LMS algorithm is its sensitivity to the scaling of its reference input. This makes it very hard to choose a learning rate that guarantees stability of the algorithm [52]. The NLMS filter solves this problem by normalizing μ with the energy of the input reference signal.

Table 4.1 describes the system equation associated with the LMS and NLMS filter algorithms used to update their filter coefficients.

Table 4.1. ANC filter equations [52].

Type of filter	System Output
LMS	$\mathbf{w}\hat{}\,(n+1) = \mathbf{w}\hat{}\,(n) + \mu\,\mathbf{u}(n)e^*(n)$
NLMS	$\mathbf{w}\hat{}\,(n+1) = \mathbf{w}\hat{}\,(n) + \frac{1}{\|\|\mathbf{u}(n)^2\|\|}\mathbf{u}(n)e^*(n)$
Filter Parameters	
w(n)	Filter weights
n	Filter Order
μ	Convergence Factor
u(n)	Input reference signal
e(n)	Error Signal

5. Statistical Parameters

Our proposed MA algorithms makes use of the statistical parameters described by Selvaraj et al [55] for classifying PPG signals using Kurtosis (K) and Shannon Entropy (SE) based on pre-defined thresholds. The computation of these parameters helps to identify corrupted PPG segments and omit them from further processing. We hypothesized that this would significantly lower the false variations in the vital parameter readings and prevent outliers in a spurious noise environment. For clarity, the two aforementioned statistical parameters are summarized below:

a) **Kurtosis (K):** Is defined as a measure of "peakedness" of a given data set around its mean. It gives an indication of a random number being assigned a value that will be close to the mean. It has been used in the past to identify fidelity of recorded ECG data [56] and is computed with the help of the equation below:

$$k = \frac{E(x-\mu)^4}{\sigma^4} \tag{5.1}$$

where, μ and σ are the mean and standard deviation of x and E represents the expected value of $(x- \mu)$.

b) **Shannon Entropy (SE):** Is used to measure the uncertainty of the desired signal and quantifies the difference in the probability distribution relative to a uniform distribution. It is computed with the help of equation:

$$SE = -\sum_{i=1}^{k} \frac{p(i) * \log(p(i))}{\log(\frac{1}{k})} \tag{5.2}$$

where, i is the bin number used to make SE a finite quantity and k is assumed to be 16 for simplicity, $p(i)$ is the probability distribution of the signal amplitude.

5.1. MNA Algorithm

The stepwise computation of K and SE from a 60 s PPG segment developed by Selvaraj et al. is shown in Figure 5.1. Initially, the signal is filtered using a 64th order bandpass filter to extract the AC component of the PPG signal. Next, the algorithm detrends the signal using a 22nd order polynomial equation in order to remove non stationary dynamics which may be present due to instrumentation lag and the subject's breathing. This detrended signal is then used to compute K using an inbuilt Matlab function and SE using a custom built function designed by [55].

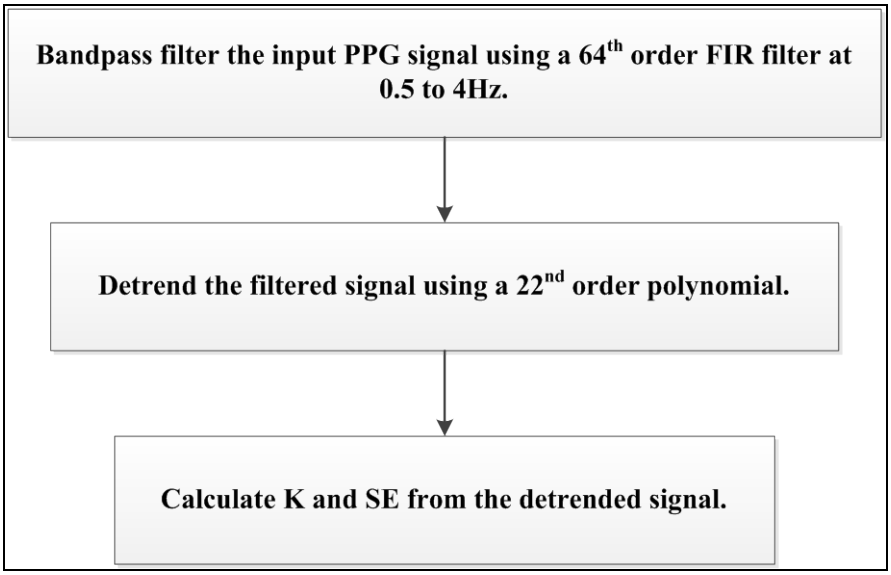

Figure 5.1. MNA algorithm flowchart designed by Selveraj [55].

As illustrated in Figure 5.2, we now propose to use this algorithm in conjunction with the HR and SpO_2 algorithms (HSA) to extract more accurate vital parameters from the data collected by the ABS sensor.

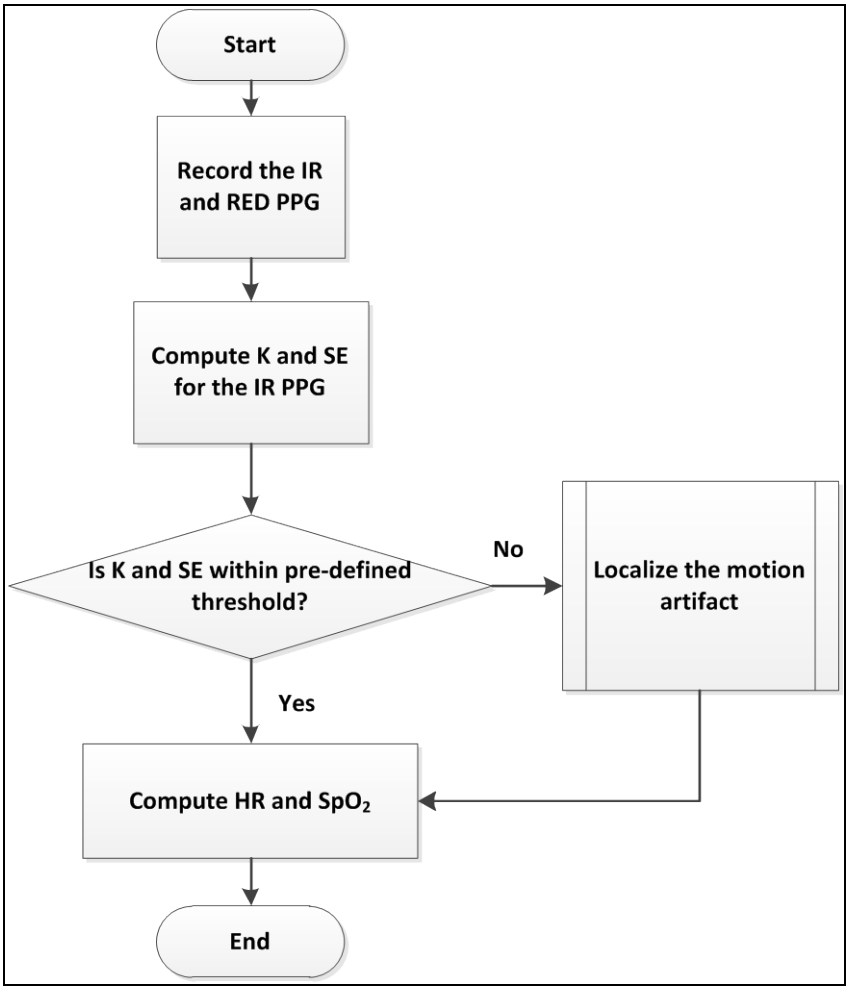

Figure 5.2. Proposed MNA algorithm flowchart.

For all our analysis, we compute the K and SE for only the IR PPG data segments while working with the hypothesis that MA equally affects both the IR and R PPG signals. Hence K and SE for either PPG should follow a similar pattern. The raw IR is inputted to the MNA algorithm which computed the aforementioned statistical parameters using the work flow shown in Figure 5.1.

If the computed values fall within the specified range then the corresponding vital parameters for those segments are calculated. However, if the statistical values were found to be above these thresholds then the segments were classified as being corrupt. The two methods (for two different algorithms) that were investigated for overcoming MA:

- Localizing spikes in the signal (MNA algorithm)
- Using ANC (MNAC algorithm)

6. Research Objectives

AIM 1: Collect raw PPG data from the ABS forehead mounted sensor to determine the ability of the MNA algorithm to detect motion artifacts in accordance with the algorithm developed by Selvaraj et al.

AIM 2: Develop a novel MA algorithm to classify the incoming PPG signal and extract the respective HR and SpO_2 values.

AIM 3: Develop an ANC-MA algorithm using a combination of statistical parameters and a NLMS ANC filter to filter the corrupted PPG segments and then extract HR and SpO_2 values.

7. Preliminary Research

7.1. Control Study

As part of our preliminary research we conducted a control study to validate the functionality of the HR and SpO_2 Algorithms (HSA) in the absence of any motion artifacts. This involved recording 5 min sitting PPG data from 5 subjects and then comparing the output values with independent reference standards.

7.1.1. Experimental Setup

The following experimental setup was used for the control study

i. Our custom designed reflectance pulse-oximeter was mounted on the forehead for collecting raw PPG data sampled at 80Hz.
ii. A benchtop ECG machine was connected on the patient's chest using 5 leads to record a 3 channel ECG data sampled at 400Hz to obtain simultaneous reference HR values.
iii. A Masimo® SET bench top finger pulse-oximeter was placed on the left index finger for simultaneous reference SpO_2 measurements.

7.1.2. Peak Detection

Initially, our aim was to assess the accuracy of the peak detection algorithm as it is the most pertinent aspect in the PPG based HR estimation. We worked on the hypothesis that there is a simultaneous ECG R wave for every PPG peak. Figure 7.1 shows simultaneous recording of typical ECG and PPG signals.

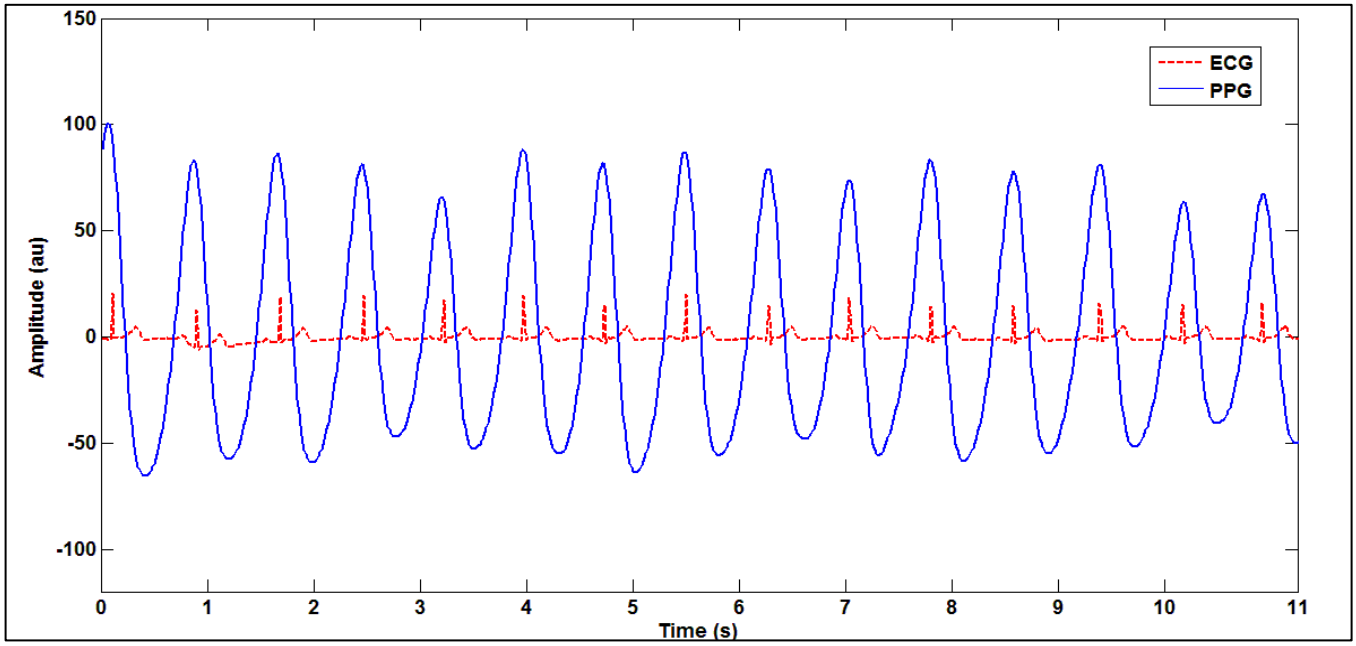

Figure 7.1. Superimposed ECG and PPG waves from a typical recording.

To assess the accuracy of our peak detection algorithm, we compared the number of PPG peaks to the number of ECG R wave peaks by performing the following operations:

i. First, the ECG data were down-sampled to from 400 Hz to 80Hz in accordance with the PPG sampling rate.

ii. Next, the PPG peaks were detected using the PPG HR algorithm.
iii. Finally, the R wave peaks were identified using an existing algorithm described by [57] and also manually inspected to eliminate any chances of false positives or true negatives.

The peaks detection results (summarized in Table 7.1) showed 100 % detection and affirmed the functionality of the PPG peak detection algorithm.

Table 7.1. ECG vs. PPG Peak Comparison.

Subject	R Peaks	False or Missed R peaks	PPG Peaks
1	391	0	391
2	370	0	370
3	247	0	247
4	289	0	289
5	425	0	425
Total	1722	0	1722

The next step was to verify the accuracy of this peak detection algorithm in terms of HR estimation as well as the existing SpO_2 algorithm with respect to established reference standards.

7.1.3. Vital Parameter Comparison

In the following sections, we analyzed the performance of the HR and SpO_2 separately.

a. Heart Rate

We compared each ECG derived HR with respect to the corresponding PPG derived HR in terms of the correlation coefficient (R^2) and limits of agreement using a Bland Altman plot. Figure 7.2 shows HR readings obtained from one of the recordings.

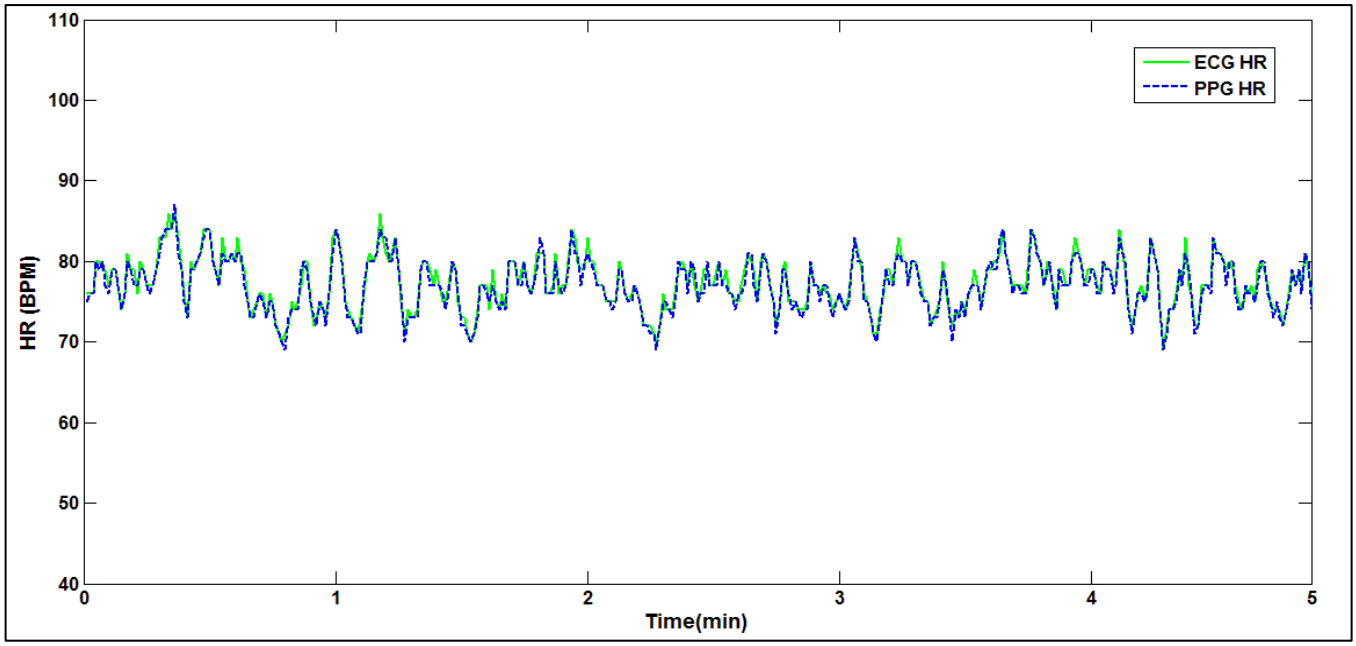

Figure 7.2. ECG vs. PPG derived HR.

A total of 1709 data points were analyzed to obtain a regression plot as shown in Figure 7.3 for the PPG and the corresponding ECG derived HRs.

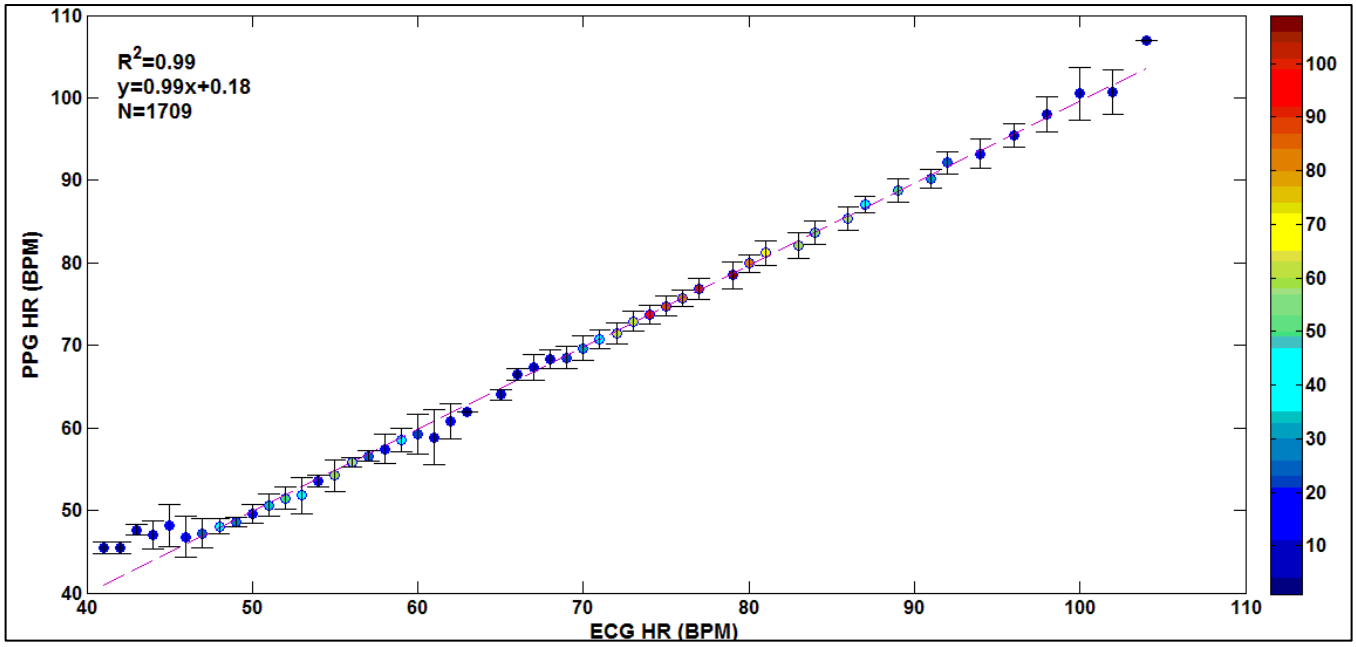

Figure 7.3. Regression plot for HR values. The color bar indicates the frequency of the data points.

Similarly, to analyze the limits of agreement between the two independent HRs we also constructed a Bland Altman plot as shown in Figure 7.4. Here, the difference HR (y-axis) was calculated by subtracting the PPG derived HR from the ECG derived HR while the average HR (x-axis) was obtained by calculating the means between the PPG and ECG derived HRs. The ±1.96 SD margin specifies the limits of agreement within a 95% confidence interval (CI) while the mean line represents the bias between the ABS sensor and the ECG monitor. We observe relatively large errors during low resting HRs in the range of 45-60 BPM whereas for values above 65 BPM no significant error points were observed.

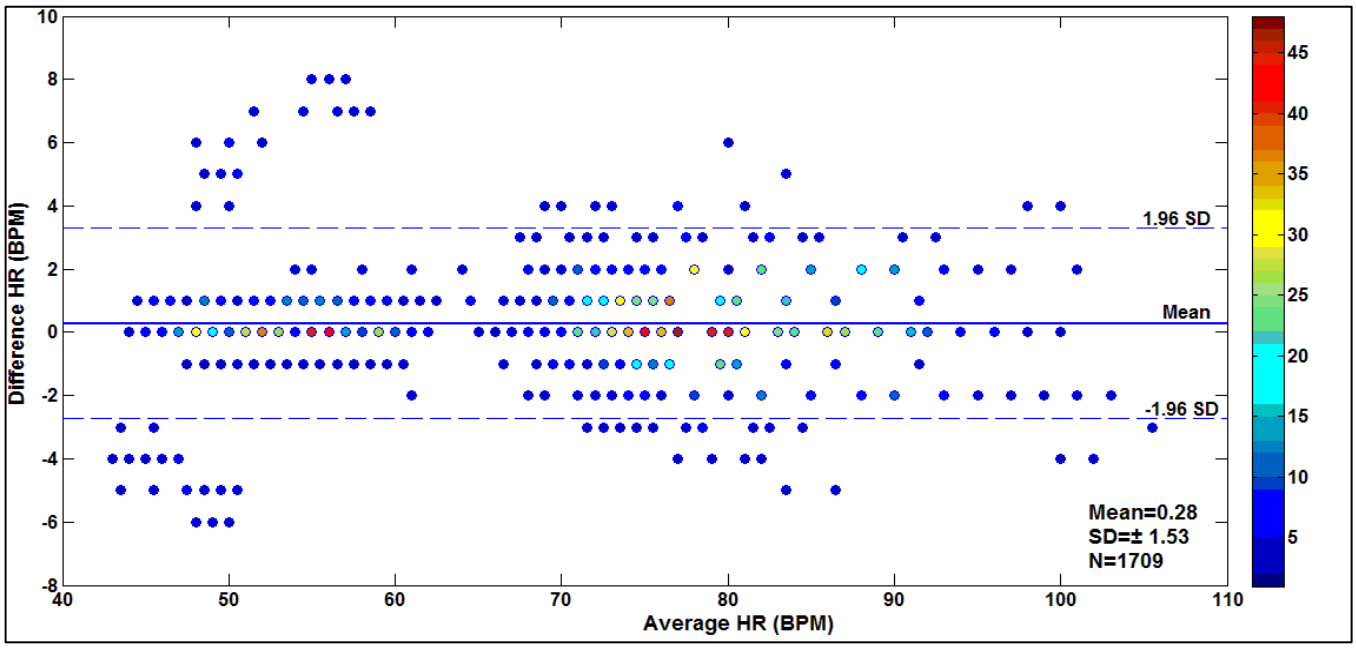

Figure 7.4. Bland-Altman plot for HR values.

b. Oxygen Saturation

Similarly, as shown in Figure 7.5, the regression plot was obtained between the PPG derived SpO_2 obtained from the ABS reflectance sensor and Masimo derived SpO_2. A total of 1426 values were analyzed, producing a R^2 of 0.86.

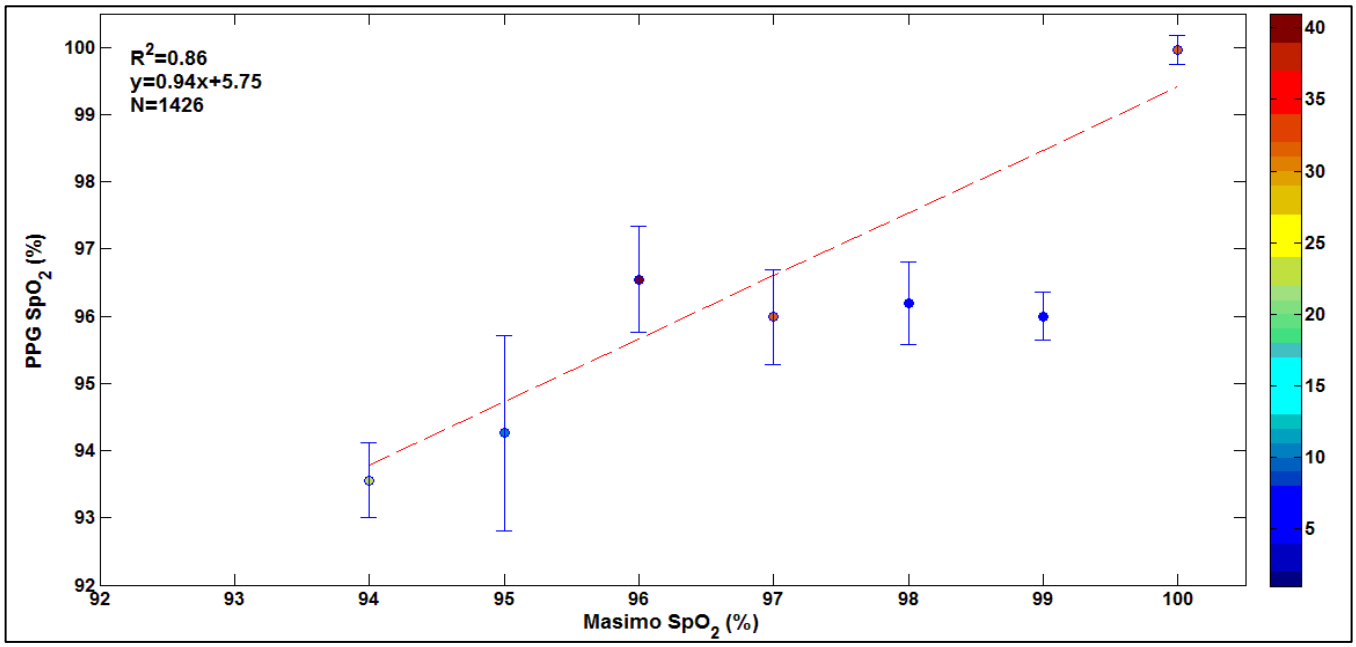

Figure 7.5. Regression plot for SpO_2 values.

In the case of Bland Altman plot shown in Figure 7.6, the difference SpO_2 was obtained by subtracting SpO_2 from the Masimo pulse oximeter whereas the average values were derived by the taking the means of both readings.

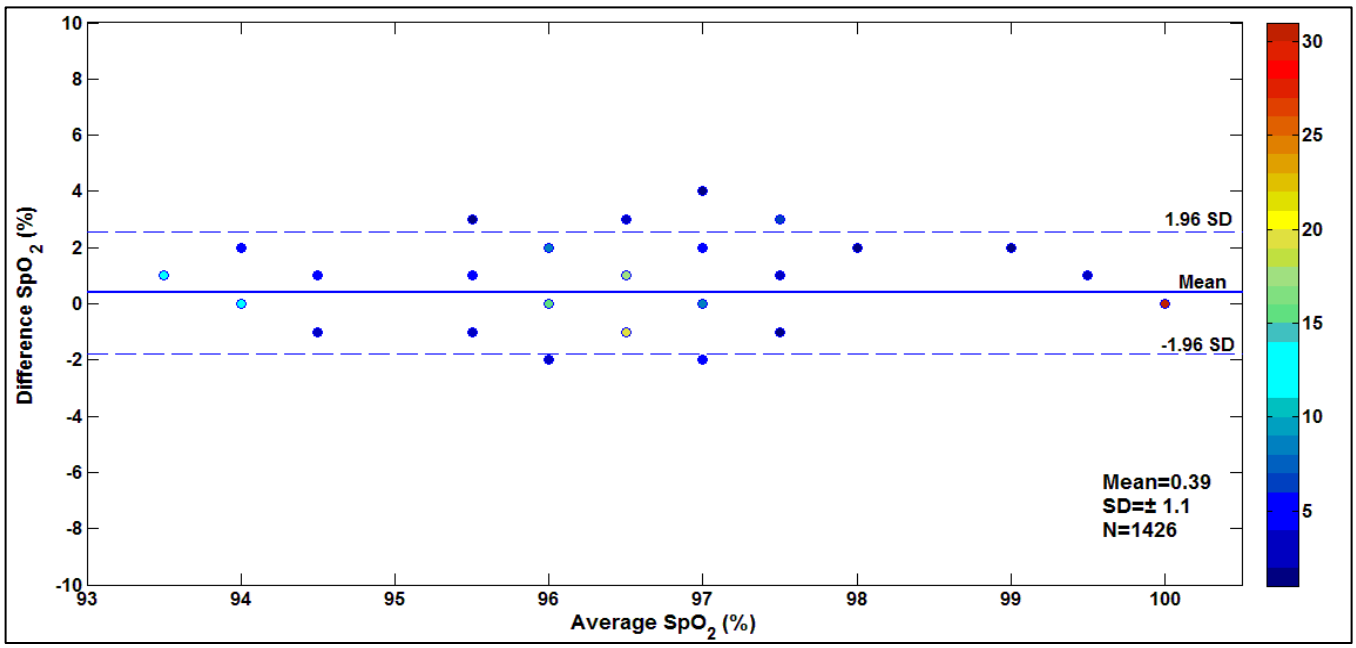

Figure 7.6. Bland-Altman plot for SpO_2 values.

The results from the control study in regard to both vital parameters are summarized in

Table 7.2. Outputs obtained from the ABS sensor showed a negligible bias of 0.28 and 0.39 compared to their reference values. Finally, the deviation of HR and SpO_2 in the regard to reference standards was found to be within ±1.53 BPM and ±1.1%, respectively.

Table 7.2. Cumulative control study results.

Vital Parameter	Total Values Analyzed	Mean Difference	SD	R^2	Points within ±1.96 SD
HR	1709	0.28	±1.53	0.99	93.15%
SpO_2	1426	0.39	±1.1	0.86	95.15%

In conclusion, we were able to successfully validate the functionality of the HSA in the absence of any motion artifacts.

7.2. Effects of MA on the ABS sensor

The next task was to investigate the performance of HR and SpO_2 algorithms (HSA) in the presence of motion artifacts. We conducted certain preliminary experiments solely with the ABS sensor. A total of 4 people wore the ABS sensor as shown in Figure 7.7 and followed the experimental protocol described in Table 7.3.

Figure 7.7. Forehead mounted sensor.

The initial test began with acquiring baseline sitting data for 3 min. Next, the subject randomly twitched their forehead in order to induce MA. To analyze the effects of head movements, the subjects shook their head in the vertical and then the sideways direction for the next two minutes. Finally, the subjects sat still in order to obtain baseline values in a resting state.

We worked on the hypothesis that the ideally vital parameter readings of healthy individuals should remain within a small range as the entire experiment was performed under rest. Any extreme changes in these values could be attributed to the effects of MA.

Table 7.3. Preliminary MA analysis protocol.

Activity	**Time**
Sitting Still	3 min
Forehead Twitching	1 min
Head Movement: [Up and Down]	1 min
Head Movement: [Left and Right]	1 min
Recovery (Sitting Still)	3 min

Figure 7.8 shows the average HR during the preliminary tests from one of the recordings. Here, the ideal HR of 45-50 BPM indicates the typical readings during rest and should be observed throughout the experiment. However, during head movements we observe a twofold increase in HR values which may indicate corrupt PPG segments rather than intensive exercise. This elevated HR indicates the presence of false peaks in the obtained IR PPG signal which may be caused by MA.

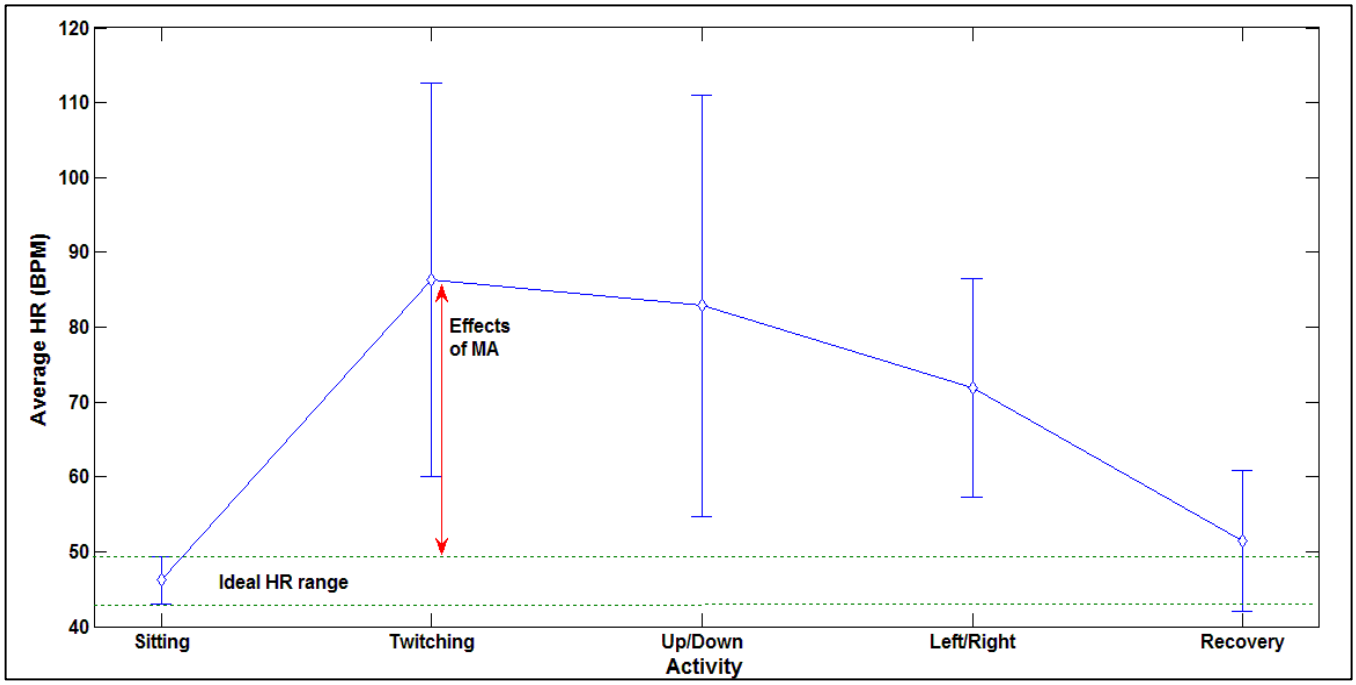

Figure 7.8. Mean ± SD HR change for different activities from one recording.

Similarly, the corresponding mean SpO_2 values from the same experiment are shown in Figure 7.9. Here the ideal SpO_2 range was considered to be recorded during rest and found to be within a 96-98%. However, subtle head movements caused large errors, with values dropping to as low as 70% in under 1 min; which again is not viable for a healthy person. These results show an inability of the algorithms to counter MA.

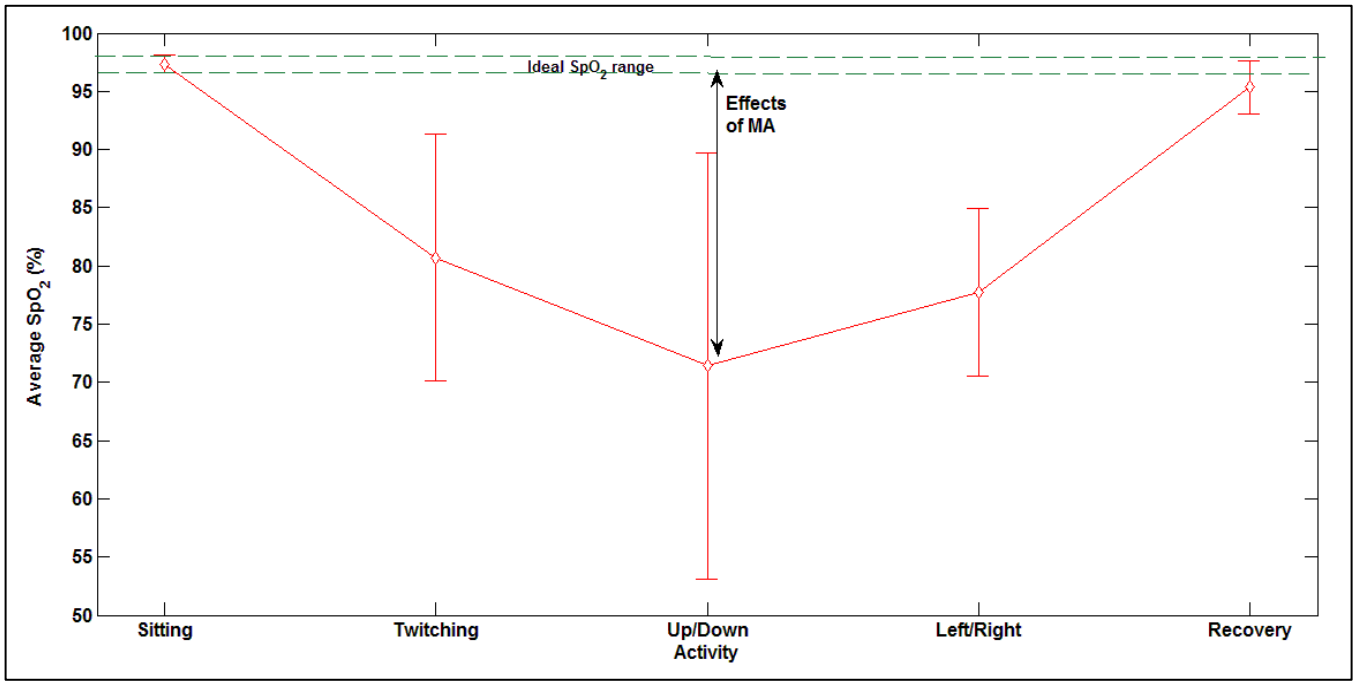

Figure 7.9. Mean ± SD SpO_2 change for different activities from one recording.

7.2.1. Cumulative Results

For the cumulative results, we analyzed the change in the HR and SpO_2 readings, when compared to the resting state for each individual separately as the resting HR and SpO_2 levels are different for every individual

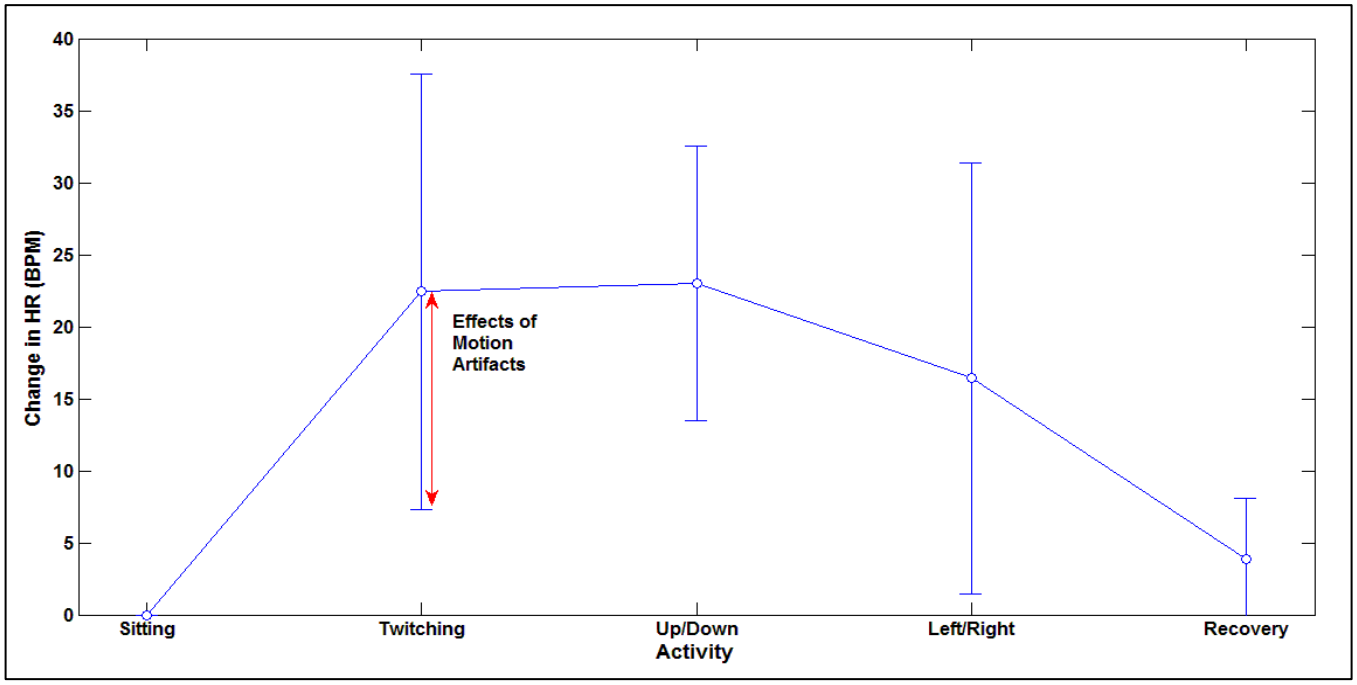

Figure 7.10. Change in average HR± SD compared to sitting average sitting values for all the datasets.

Figure 7.10, shows the mean absolute value change of HR readings for different activities when compared to the average sitting HR. We observed an average change in of 20±15 BPM during the various head movement that clearly showcases the adverse effects of MA.

Similarly, Figure 7.11 shows the mean absolute change for SpO_2 values compared to values during rest should remain unchanged. As mentioned in section 3.1, ideally SpO_2 should only change by 2-3% during strenuous exercise. However, here we again observe an average change of 15±10% during vertical and horizontal movement in fewer than 60s which again indicates the effects of MA.

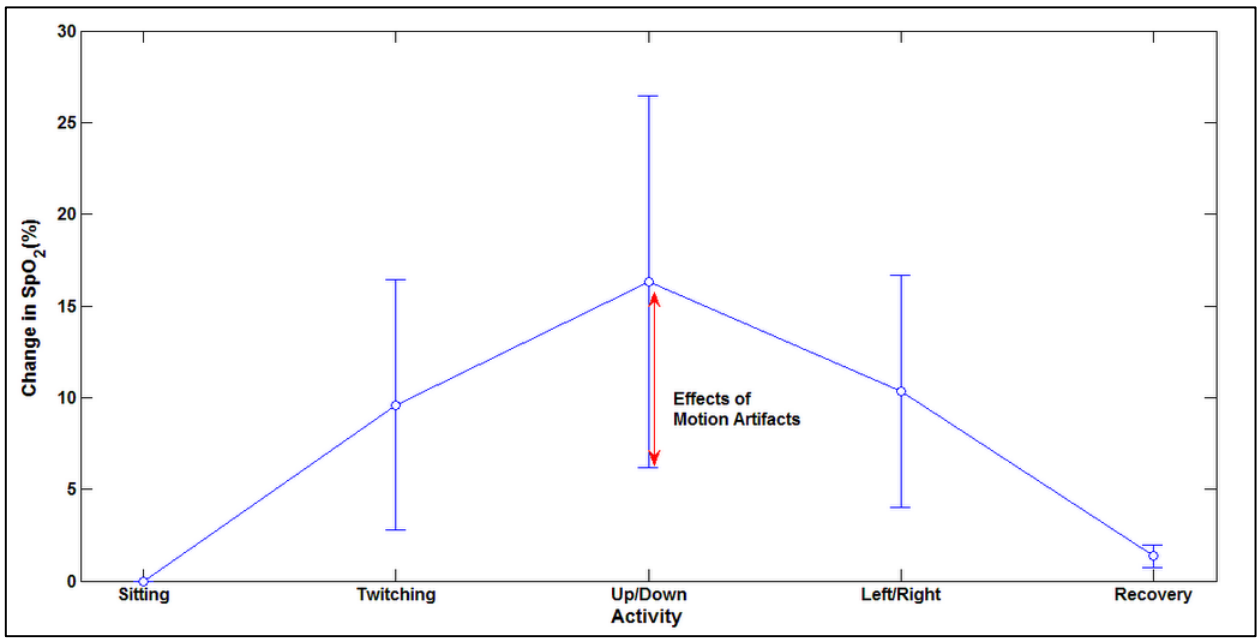

Figure 7.11 Average ± SD change in SpO_2 compared to average sitting values for all the datasets

To address some of these challenges we now investigate the use of MNA algorithm to minimize some of these effects. The next step was to investigate the possibilities of integrating these algorithms with the MNA algorithm described in chapter 5.

8. Preliminary Analysis of the MNA Algorithm

This work was aimed towards the completion of the first research objective. Here, the functionality of the original design of the MNA algorithm using 60 s PPG data segments was tested using raw PPG data collected from our forehead mounted ABS sensor. The focus here was to assess if the algorithm could accurately detect motion artifacts present in the PPG signal for different outdoor activities. Data were collected from 5 subjects and results obtained from the MA algorithm were analyzed offline using Matlab v.2011a.

8.1. Experimental Protocol

Raw IR and R PPG were recorded from 5 people following the protocol shown in Figure 8.1. Each activity was performed for 5min; '*' indicates that data recording during rest (sitting) was performed both in the beginning and the end of the experiment.

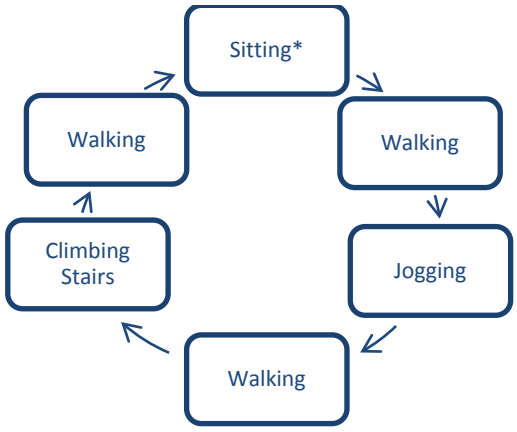

Figure 8.1. Preliminary experimental protocol

IR and R PPGs were recorded using a laptop computer which was placed inside a backpack and worn by the subject during the entire experiment.

8.2. Preformatting Data

The collected data needed to be first pre-formatted before computing its K and SE values. This involved segregating the data into 60 s segments, where each segment was shifted by 10 s with respect to the previous segment. The hypothesis here was that this approach would help in localizing motion artifacts. Next, the corresponding K and SE values were calculated for each segment and stored in a database.

8.3. Visual Identification of Corrupted Segments

Next, we visually inspected all segments to detect the presence of any spikes or abnormal amplitude variations. If any spurious variations were detected, then the segment was classified as 'corrupt' and its corresponding K and SE values were saved into a separate database. Similarly, if a segment contained a recognizably clean PPG data it was classified as 'clean' and its values were noted down separately. The results from the visual inspection are summarized in Table 8.1. Note that the visual inspection of segments was undertaken by 3 individuals separately. Only those segments which were commonly identified by at least 2 observers were classified as being 'corrupt'.

Table 8.1: Results obtained from visual inspection of PPG data segments from the 5 recordings.

Dataset	Total Number
Total Number of Data-segments	936
Clean Data Segments	525
Corrupt Data Segments	411

8.4. Receiver Operating Characteristics (ROC)

In order to determine the optimal threshold for both parameters we performed a ROC test with the help of Sigma plot 11.0 software using a 95% CI. Note, that both K and SE were considered individually.

The classification criterion in terms of the ROC was followed in accordance with [55] with the specificity and sensitivity given by:

a) **Specificity (Sp)**

- Described in terms of the clean segments by the following equation:

$$\mathbf{K_i <= K_{TH};}$$

where K_{TH} is the threshold value that was varied from 2-10 by following the protocol described in [55] .

- Described in terms of clean segments by the following equation:

$$\mathbf{SE_i >= SE_{TH};}$$

where SE_{TH} was the threshold varied from 0.2 to 1 by following the protocol described in [55] .

b) **Sensitivity (Se)**

- $K_i > K_{TH}$ were classified as corrupt.
- $SE_i < SE_{TH}$ were classified as corrupt

Here i= [1,936];

In terms of a mathematical equation Se and Sp are defined as:

$$\text{Specificity(Sp)} = \frac{\text{Number of Clean Segments}}{\text{Total Number of Clean Segments}} \quad (8.1)$$

$$\text{Sensitivity(Se)} = \frac{\text{Number of Corrupt Segments}}{\text{Total Number of Corrupt Segments}} \quad (8.2)$$

The ROC results obtained for both K and SE during the study were as follows.

i. **K**:

a. Sp and Se curves obtained for K are shown in Figure 8.3 along with the area under the ROC curve, which was found to be 0.97.

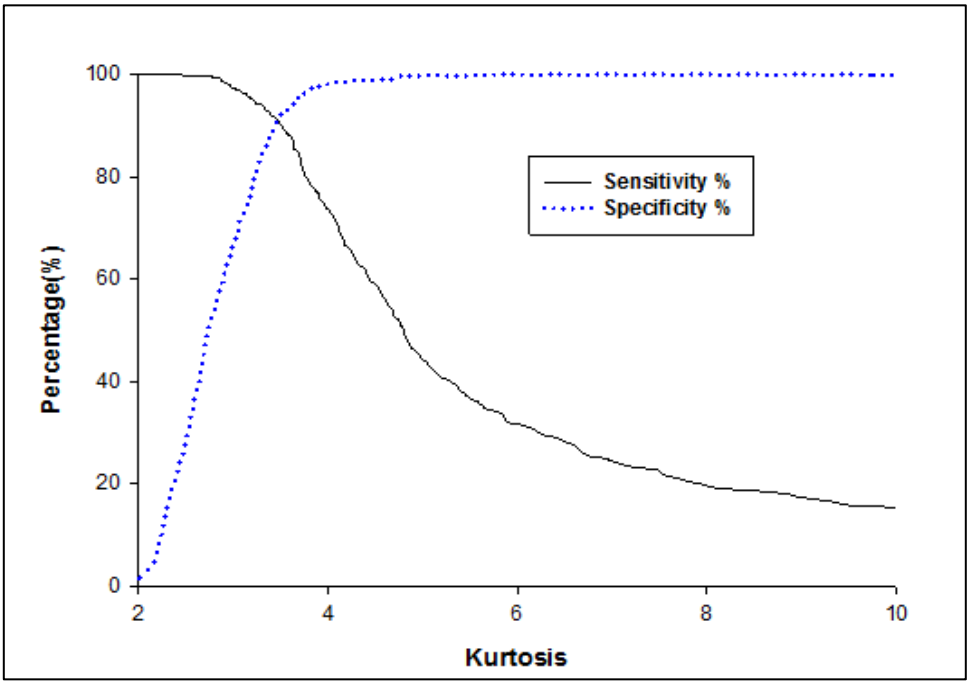

Figure 8.2. The specificity and sensitivity for K.

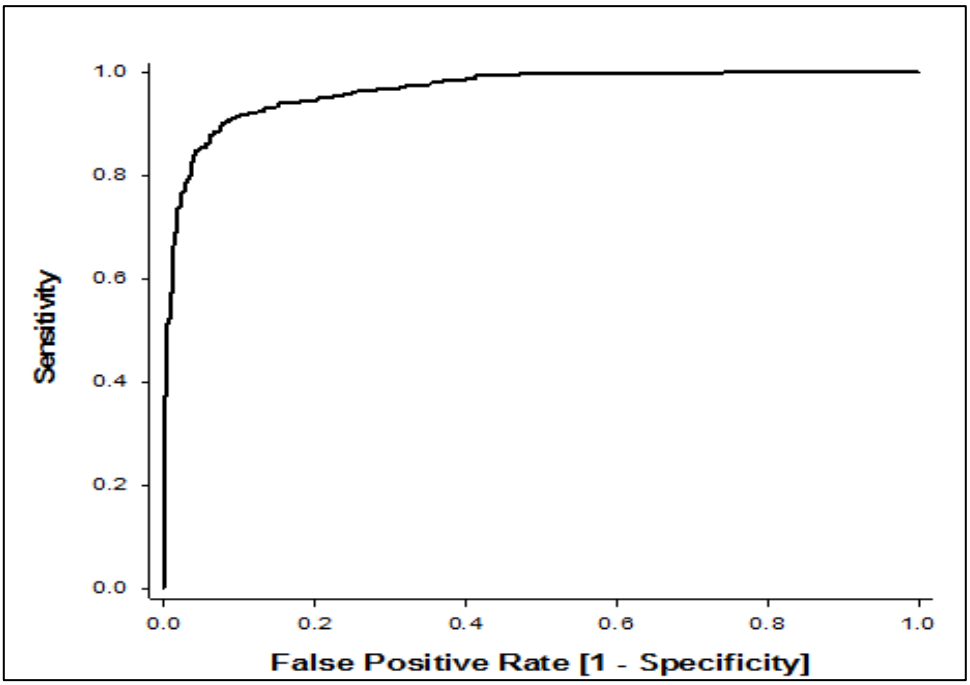

Figure 8.3. Area under the ROC curve for K.

b. To obtain a range of K values for both the clean and corrupt datasets, we constructed a box plot as shown in Figure 8.4. Here, the mean values for the clean and corrupt data were found to be 2.82 and 9.81, respectively.

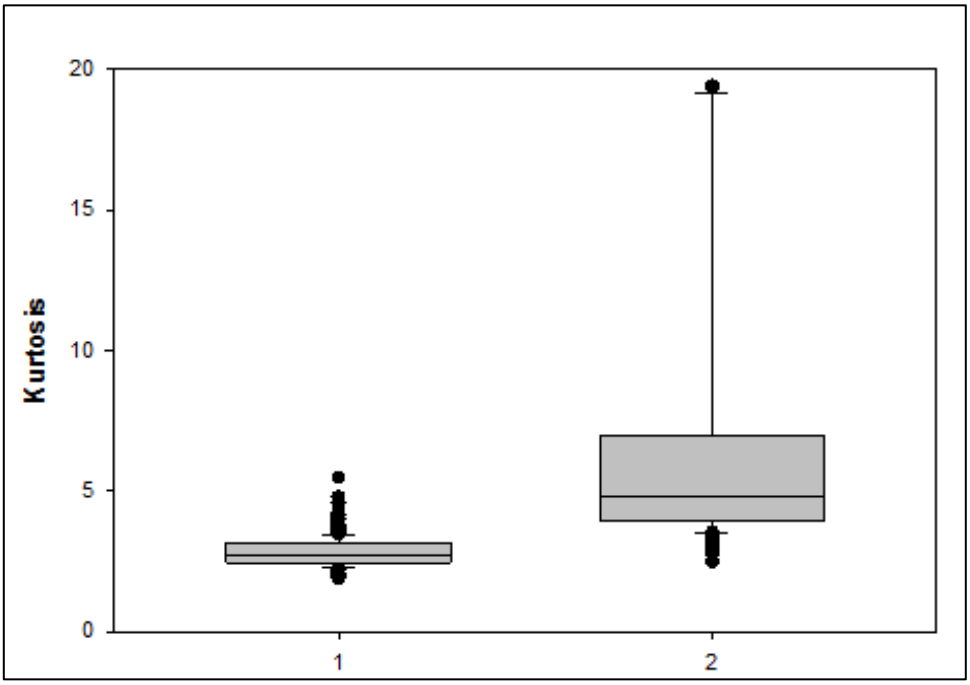

Figure 8.4. Box plot for K; 1 represents clean data and 2 corrupt data.

ii. **SE**

Sp and Se curves along with the area under the ROC curve (which was found to be 0.95) are shown in Figure 8.6.

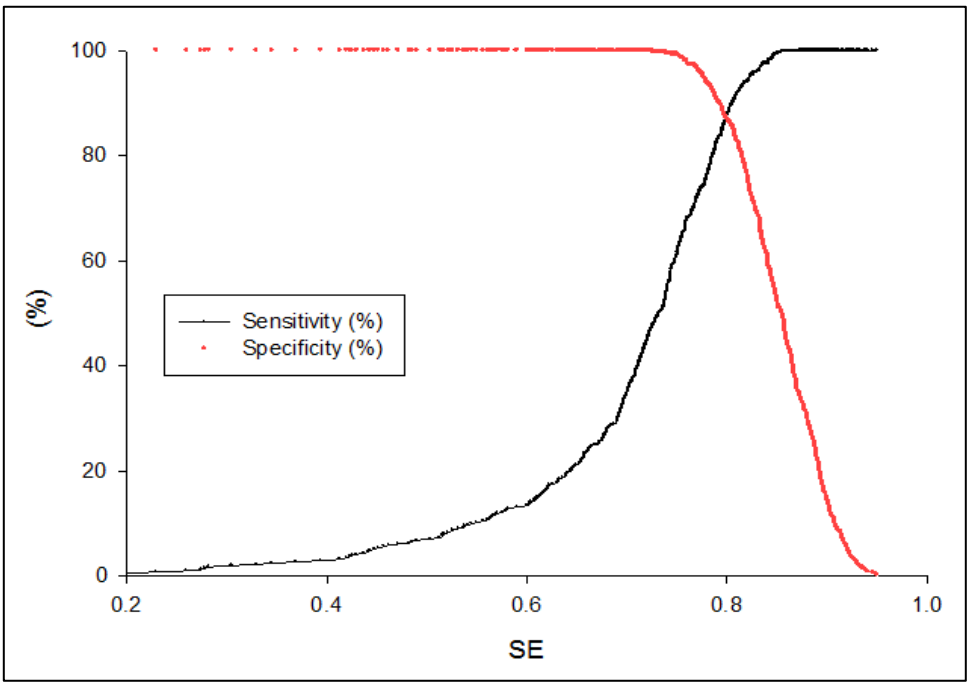

Figure 8.5. The specificity and sensitivity for SE.

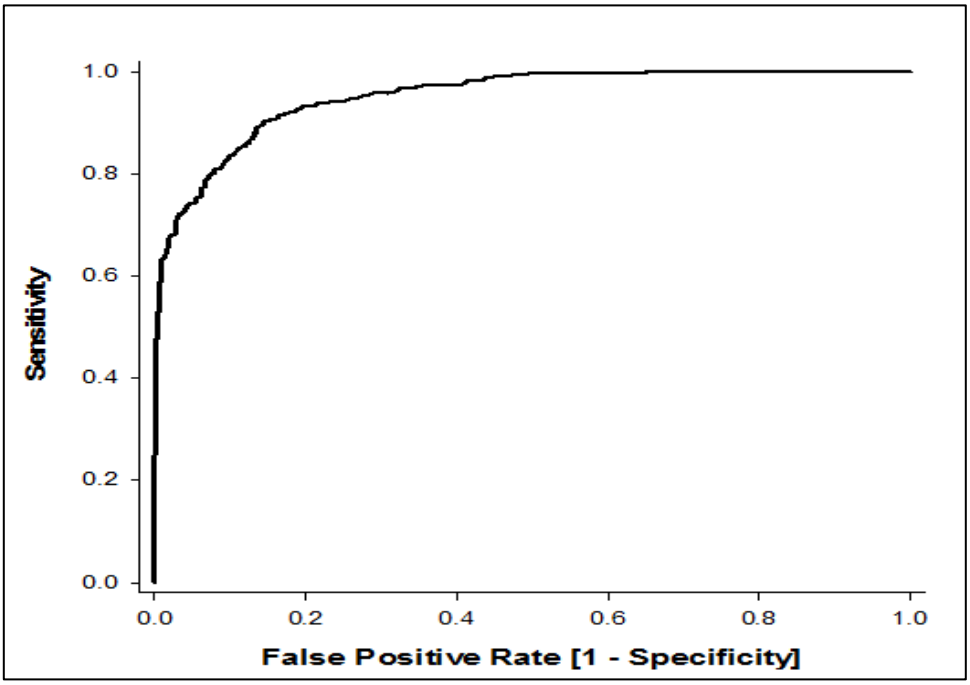

Figure 8.6. Area under the ROC curve for SE.

To obtain a range of SE values for both the clean and corrupt datasets, we constructed a box plot as shown in Figure 8.7. Here, the mean SE value for clean and corrupt data was found to be 0.85 and 0.70, respectively

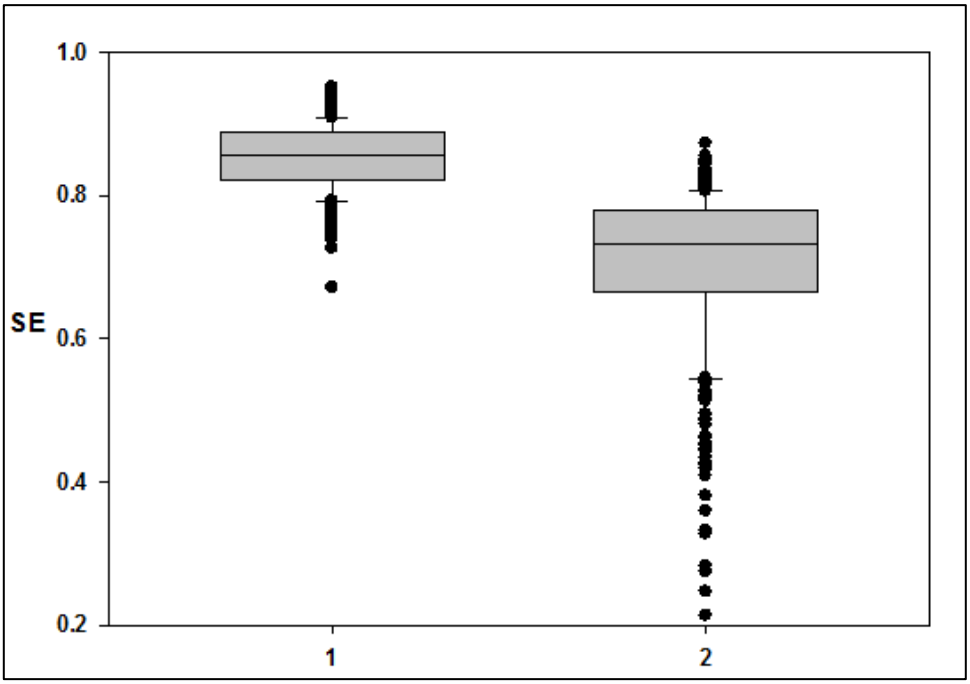

Figure 8.7. Box plot for SE, 1 represents clean data and 2 corrupt data.

The cumulative ROC results for both the statistical parameters are summarized in Table 8.2. The accuracy refers to the number of clean and corrupt segments divided by the total number of segments at these particular thresholds.

Table 8.2. ROC results for 60s PPG data segments.

	SE_{TH}= 0.80	K_{TH}=3.46	K_{TH} and SE_{TH}
Specificity (%)	**86.8**	**90.6**	**84.76**
Sensitivity (%)	**87.3**	**91.0**	**85.64**
Accuracy (%)	**87.07**	**90.8**	**85.15**

The chosen threshold values for all future classification for the data collected on the ABS sensor as shown in Table 8.3.

Table 8.3. Criterion for Classification

Clean PPG Data	$K \leq 3.46$ and $SE \geq 0.80$
Corrupt PPG Data	K>3.46 and SE< 0.80

8.5. Results

The cumulative classification results obtained by processing the five recorded datasets using the selected thresholds are shown in Figure 8.8.

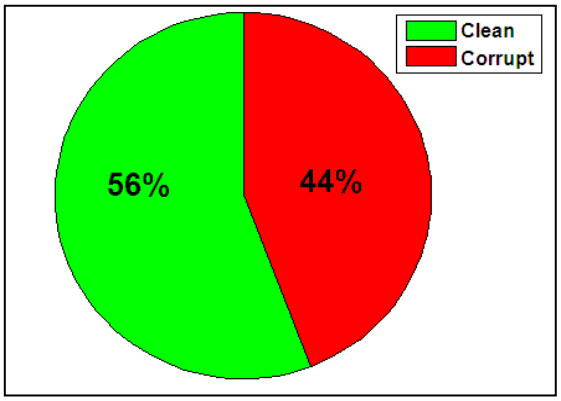

Figure 8.8. Cumulative results obtained from preliminary testing.

To get a distribution of K and SE values for all the 5 datasets, we individually constructed the histograms for clean and corrupted K and SE data separately. Figure 8.9, shows the histograms for K values obtained from the clean and clean corrupted segments. We observe that clean K ranges is distributed from 2 to 3.5 with some outliers consist of values greater than 4, on the other hand the corrupted K values are consistently greater than 4.

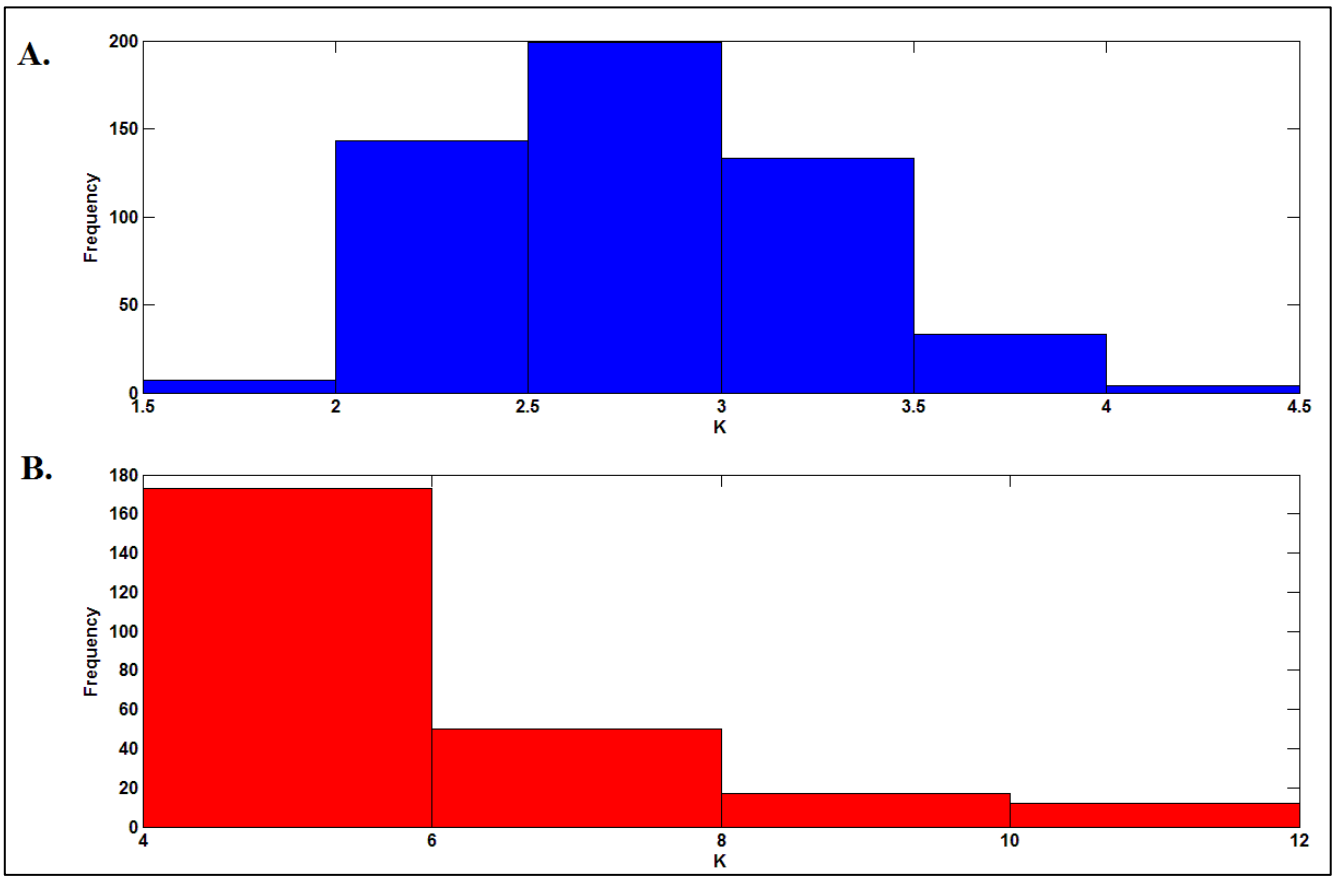

Figure 8.9. Clean (A) and Corrupted (B) K histograms.

Similarly, Figure 8.10 shows the SE distribution for the corresponding clean data that is concentrated along the 0.8 to 0.9 range while the corrupted segments have computed SE values consistently less than 0.8.

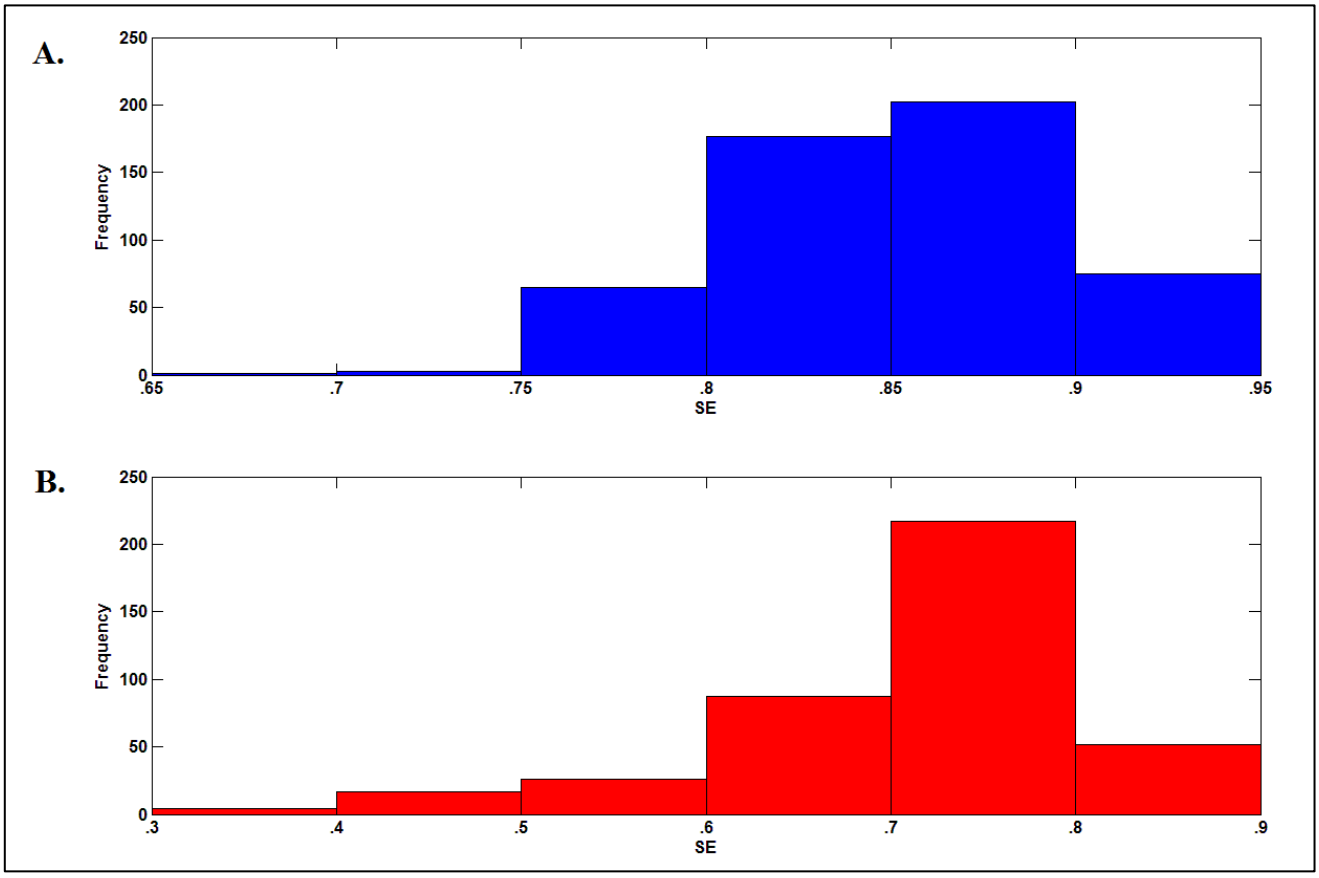

Figure 8.10. Clean(a) and Corrupted (B) SE values.

This concluded the preliminary testing of the MA algorithm. The results showed that the algorithm was indeed able to detect artifacts present in the PPG recorded by the forehead sensor. These thresholds now would form the benchmark for future classification of PPG signals. Our next goal was to combine this approach with the vital parameter algorithms as part of objectives 2 and 3.

9. MNA Algorithm

This work was aimed towards objective 2 and involved the development of the MNA in conjunction with the existing ABS sensor's HR and SpO_2 algorithms.

9.1. Initial Design

For the initial design, we collected PPG data from 7 different subjects using the same experimental protocol, as shown in Figure 8.1. The objective was to only process segments which satisfied the threshold values for both K_{TH} and SE_{TH} as specified by Table 8.3. Figure 9.1 and 9.2 show the classification results from each recording individually as well as cumulatively.

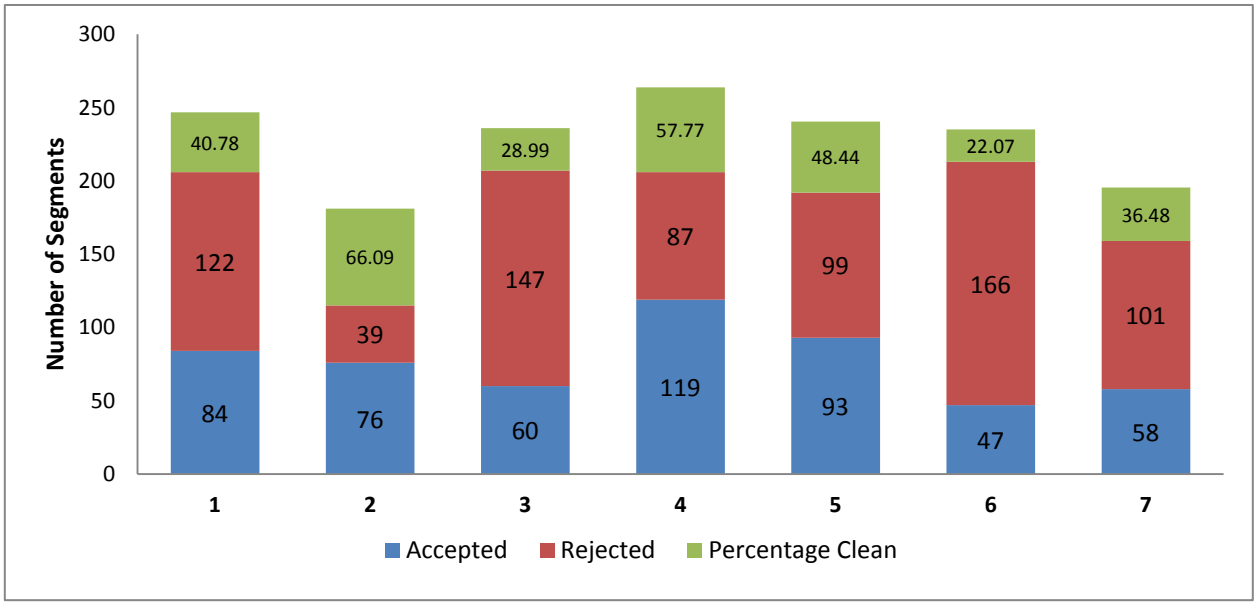

Figure 9.1. Clean and corrupt segments for the 7 recordings.

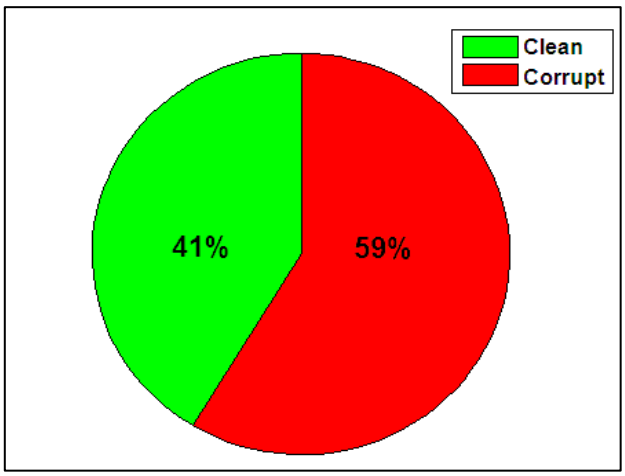

Figure 9.2. Cumulative results using the classification criterion.

From Figure 9.2, it became evident that having only a single classification criterion led to a majority rejection of data, so steps needed to be taken in order to minimize this data loss. Therefore, the process of splitting segments was developed for our algorithm which focused on simultaneously processing the rejected segments by segregating the motion artifact spikes.

9.1.1. Split Segment Approach

The focus here was on splitting the segment into two equal parts and then localizing abnormal peaks/troughs by separately computing the K and SE values for each new segment. This process can be best explained with the help of the Figure 9.3 that shows a 1 min raw PPG data segment corrupted due to the abnormal amplitude change (highlighted in red) and K and SE foe values which are above the designated thresholds.

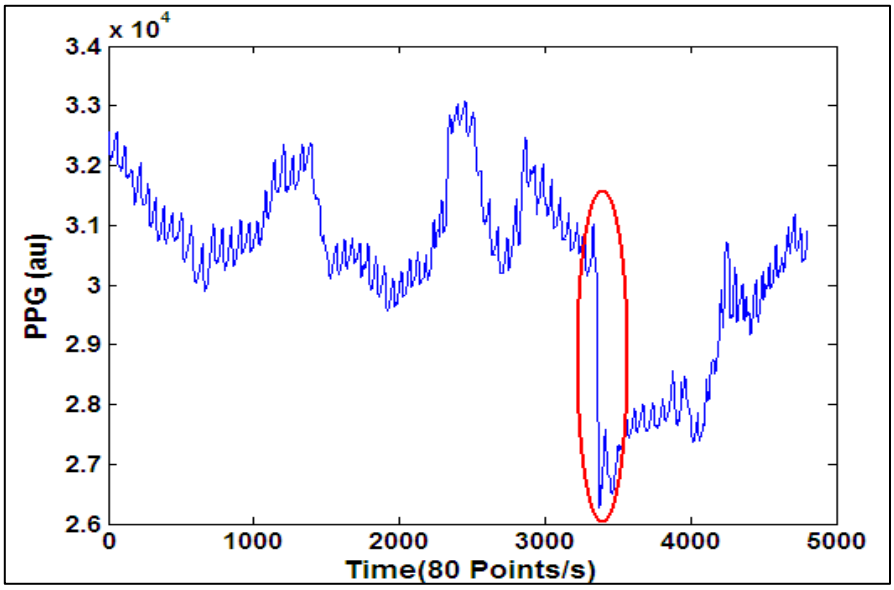

Figure 9.3. A typically corrupted PPG segment.

Using the splitting segments approach, the corrupted segment was first split into two equal 30 s segments. Then K and SE values were computed for each segment. Figure 9.4 shows the first segment with its corresponding K and SE values. These values indicate that the segment contained clean PPG data and was then used for HR and SpO_2 computation.

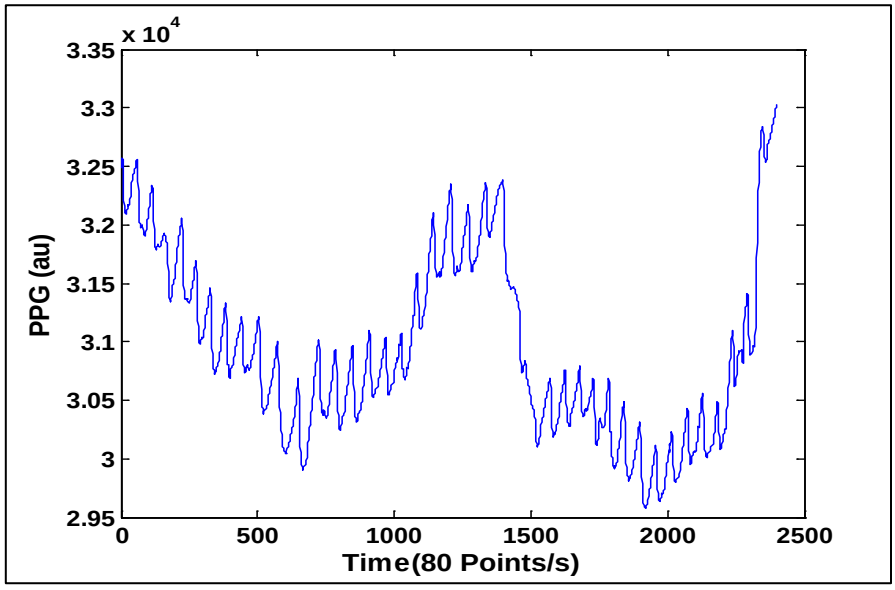

Figure 9.4. Clean PPG segment with K=2.44 & SE=0.89.

The remaining 30 s segment, shown in Figure 9.5 had highly variant K and SE values and was rejected from further computation.

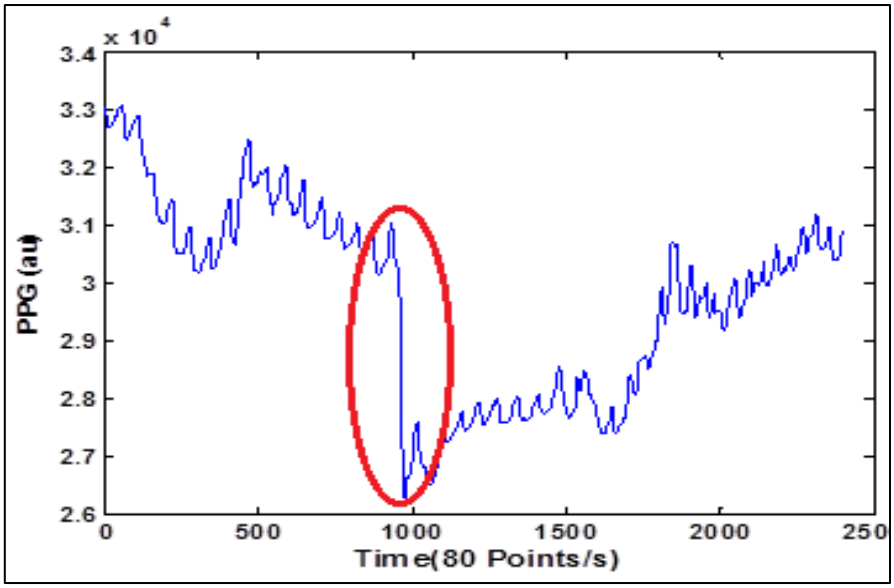

Figure 9.5. Clean PPG segment with K=9.89 & SE=0.62.

By using the split segments approach we were effectively able to minimize the percentage of segments that were out rightly rejected. Figure 9.6 shows the total number of segments (%) that were used fully or in part for computing HR and SpO_2. The rejection % indicates the segments that were completely corrupted by MA and not used for computation of any aforementioned vital parameters.

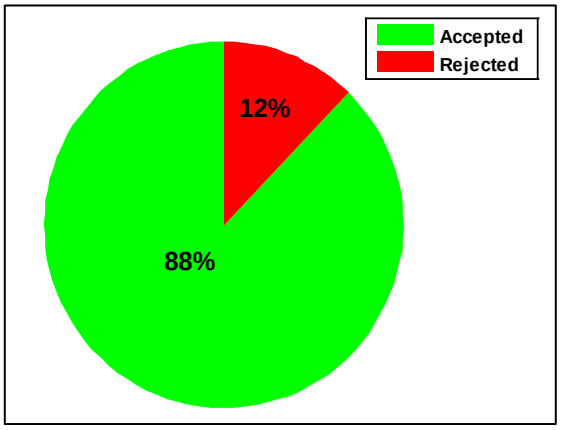

Figure 9.6. Segment accepted after split segments approach.

9.1.2. Computing HR and SpO_2

As the amount of rejected data was sufficiently reduced, the next step was to combine the novel MNA algorithm with the ABS sensor's algorithm for computing HR and SpO_2. However, this proved to be a cumbersome task as the existing algorithm was designed to process only 0.5 s of PPG data per iteration. Therefore, inputting 60 s PPG data at once lead to slower processing speed as well as repetitive output values due to overlapping regions (50s of PPG data was overlapped) between successive segments. Hence, certain steps needed to be taken in order to obtain a single vital parameter values per segment:

1. A total of 60 values were obtained for HR and SpO_2 per segment.
2. These values were curtailed using a 3 point non-overlapping median filter to reduce the output to 20 values per segment.
3. Finally, the median HR and maximum SpO_2 were selected from the 20 values as the final output.

Typical SpO_2 and HR outputs obtain from the initial design of the MNA algorithm are shown Figure 9.7 and Figure 9.8. The current sensor values in the these figures reflect the outputs from current sensor MA rejection algorithm (CSA) embedded in the ABS sensor which relies solely on moving average filters to counter MA while 'New MA' indicate MNA algorithm outputs. Note, that the values obtained from CSA (2 values per second) were downsampled by 20 in order to match with number of outputs for the MNA algorithm (1 value per 10 sec)

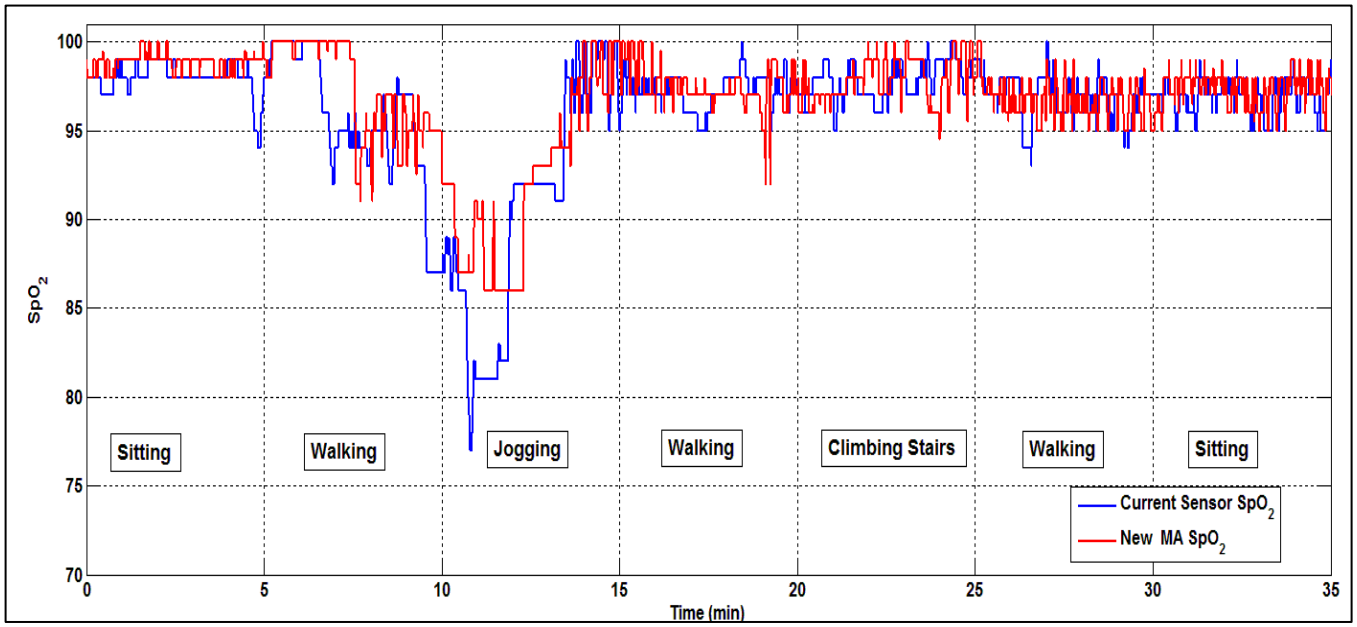

Figure 9.7. New vs. Old SpO_2 recording.

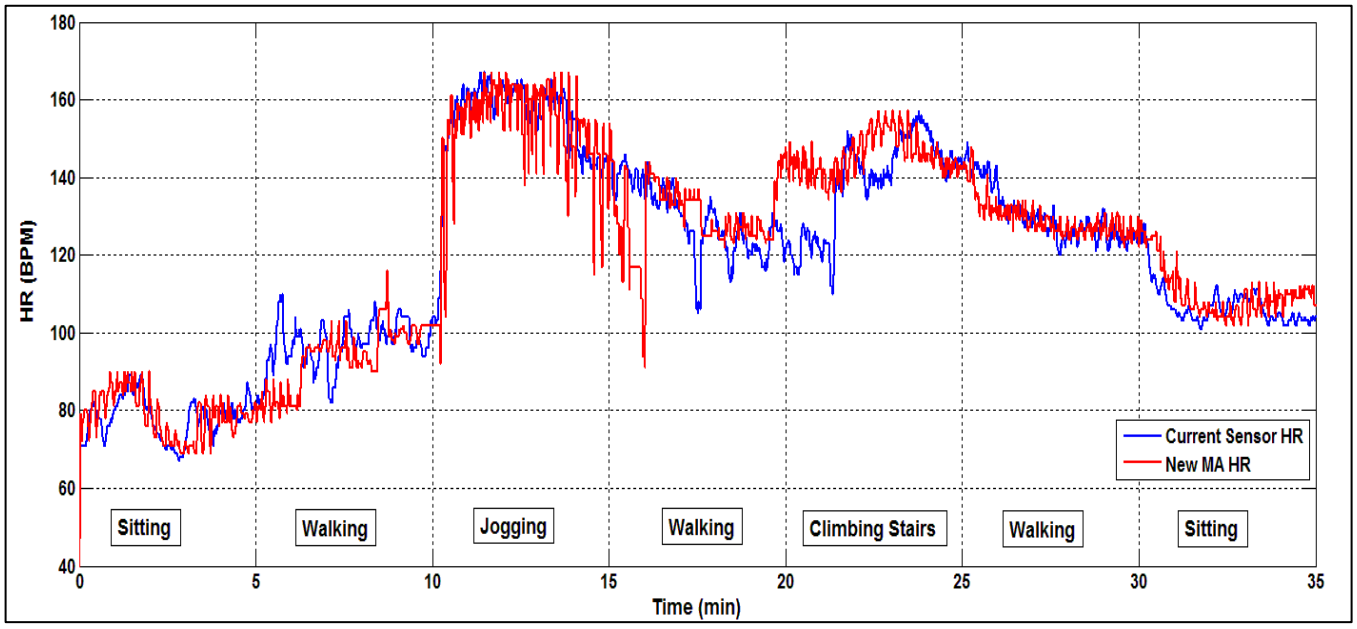

Figure 9.8. New vs. Old HR recording.

9.1.3. Drawbacks of the Initial Design

Despite the successful design and integration of the MNA algorithm with the HSA, there were still certain concerns regarding the frequency of outputs and its future implications which were:

a. As the PPG segments were shifted every 10 s, therefore the HR and SpO_2 readings were only updated after every 10 s. This approach led to concerns regarding the feasibility of the algorithm as commercial devices update their readings every second.
b. The process of outputting a HR and SpO_2 single value from 1 min PPG data had certain limitations as many physiological changes can occur in the body in a minute and a single value may not be able to fully indicate a broad clinical perspective.
c. Lastly, queuing 1 min of raw IR and R PPG data required a microprocessor memory in excess of 500 bytes that was currently unavailable in the ABS sensor. Hence R/T implementation of this algorithm would have proved to be a difficult task.

9.2. Modified Design

The concerns regarding of the initial design led to the modification in the length of the PPG data segments that were processed by the algorithm. The modified design processed 10 s PPG segments instead of the initial 60 s segments. The length was chosen in order to input minimum data length required by the HSA to output accurate data as well as maintaining the statistical efficiency of K and SE. The reduction in the minimum data length would also help reduce processing time for the MNA algorithm and avoid long delays between successive readings.

As the segments lengths were curtailed, a new ROC was performed using the 5 preliminary datasets following the same procedure described in section 8.4. Table 9.1 summarizes the threshold values obtained from the new ROC using 10 s PPG data segments.

Table 9.1. ROC results for 10 s PPG segments.

	K=3.30	**SE=0.85**	**Both K and SE**
Specificity (%)	94	90	89.7
Sensitivity (%)	87	82	80.14
Accuracy (%)	94.3	90.4	88.3

Due to the high Sp, Se and accuracy obtained for the K (in comparison to SE), we decided to use a single statistical parameter as shown in Table 9.2 for all future PPG data classification in our novel MA algorithms.

Table 9.2: New classification criterion

Criterion for Classification	
Clean PPG Data	$K \leq 3.30$
Corrupt PPG Data	$K > 3.30$

9.2.1. System Performance of the MNA algorithm

This was undertaken to determine the ideal segment shift that should be used in the MNA algorithm in order to achieve maximum accuracy. The PPG data collected from the control study (Chapter 7.1) was again processed by the MNA algorithm and the obtained HR and SpO_2 values were compared to their corresponding reference ECG and Masimo values (which were also downsampled accordingly in order to match size of the output). Finally, an error coefficient was calculated using the following equation:

$$\text{Error}(\%) = \sum \frac{|\text{Ref} - \text{Mes}|}{\text{Ref}} * 100 \qquad (9.1)$$

In the case of HR error calculation,

Ref: ECG HR,

Mes: MNA algorithm HR values.

In the case of SpO_2 error calculation,

Ref: Masimo SpO_2 values,

Mes: MNA algorithm SpO_2 values.

Table 9.3 and Table 9.4 summarize the obtained error (%) for both the HR and SpO_2. The 1 s and 5 s data shifts lead to a large of amount of error due to too little or too much overlapping of PPG data when compared to other subsequent segments. Also, the percentage of errors for SpO_2 was much less compared to HR due to its less variability.

Table 9.3. Absolute error (%) for HR determination

	Segment Shift Length				
Subject	**1s**	**2s**	**3s**	**4s**	**5s**
1	3.01	3.01	3.04	2.74	3.02
2	2.64	2.59	2.39	2.33	2.24
3	3.19	2.96	2.85	2.67	2.88
4	3.1	3.01	2.97	2.6	3.01
5	3.6	3.52	3.43	3.3	3.79
Mean	3.11	3.02	2.94	2.73	2.99

Table 9.4. Absolute error (%) for SpO_2 determination

	Segment Shift Length				
Subjects	**1s**	**2s**	**3s**	**4s**	**5s**
1	0.57	0.57	0.57	2.51	1.56
2	1	1	0.11	1	1
3	2.03	2.04	0.11	1	2.05
4	0	0	0	0	0
5	1.29	0.22	0.23	0.23	0.23
Mean	0.98	0.77	0.20	0.95	0.97

The overall error for each shift was obtained by computing the average of the mean errors between for each shift length between both the vital parameters and is summarized in Table 9.5. Therefore, we decided to implement a 3 s shift window for the final MNA algorithm as it corresponded to the lowest error.

Table 9.5. Averaged absolute error (%)

	1s	**2s**	**3s**	**4s**	**5s**
Cumulative Error (%)	2.04	1.92	1.57	1.84	1.98

9.3. Final MNA Flowchart

The final MNA algorithm obtained from combining the modified design and HSA is shown in Figure 9.9. The execution of the algorithm is described in terms of a potential R/T usage.

A. Initial execution

1. Firstly, the IR and R PPG data are queued for 10 s and the corresponding K value for the IR PPG is computed using the process described in Figure 5.1.
2. If the K values lie within the threshold (summarized in Table 9.2) then HR and SpO_2 values are computed for the current segment; else we rely of Abnormal Signal Amplitude Detection (ASAD).
3. ASAD works on the hypothesis that abnormal amplitude changes present in the signal are caused by MA and that leads to an aberrant K value. Therefore, in order to minimize data loss and frequently update the vital parameter readings, this method identifies the maximum slope of the corrupted IR-AC PPG and outputs the signal immediately before or after this slope depending on its location. This signal is then used by HSA for computation of HR and SpO_2.

B. HR and SpO2 Computation

1. Once IR-PPG data was inputted into the HSA, these algorithms compute approximately 8-10 values for both HR and SpO_2 and select the median HR, termed ‘IHR’ and the maximum SpO_2 values termed as ‘$ISpO_2$’.
2. *In order to prevent the risk of false outputs, IHR and $ISpO_2$ values are subjected to the output range condition before the final processing stage. We determined the range by processing the 7 recordings, these are:

   $(IHR - (HR\_Threshold)) \leq \pm 35$

   $(ISpO_2 - (SpO_2\_Threshold)) \leq \pm 15$

   If however, these conditions are not found to be true, then the previous HR and SpO_2 readings are considered for further processing.
3. Once the above condition are satisfied; then these newly computed values are inputted into a 5 point moving average filter to obtain final HR and SpO_2 for the respective PPG segment. These readings also form the HR and the SpO_2 thresholds which are used for the next iteration.

**This condition is only initialized after 10 iterations. Until 9 iterations, IHR and Ispo2 readings are directly inputted into the moving average filters which update the HR_Threshold and SpO_2_Threshold.*

C. The PPG data segment is then shifted by 3 s and the entire process is repeated till the sensor is power off.

D. Reset Condition

Note, incase K values for 10 consecutive segments are found to be above 3.3, then all the threshold values are reset to 0 and the algorithm is reinitialized. This is done in order to avoid stagnation of outputs readings.

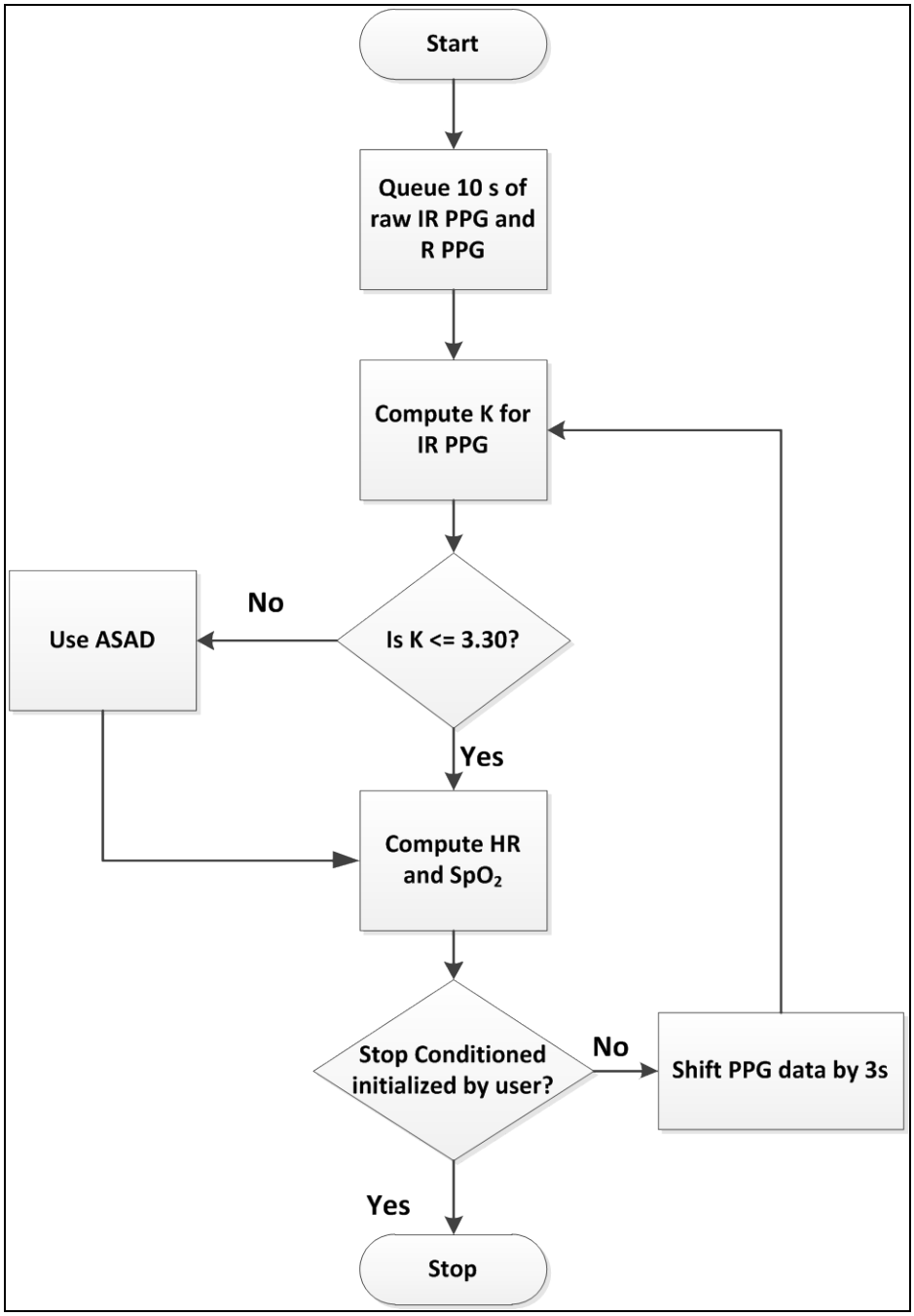

Figure 9.9. Final MNA algorithm flowchart.

10. MNA ANC Algorithm

This work was aimed at objective 3 and investigated the possibility of developing an algorithm termed 'MNAC' using K as a means of triggering ANC filtering the corrupt PPG segments.

As mentioned earlier in the report, ANC filters had been previously studied in our lab in order to investigate the possibility of R/T implementation on the ABS forehead sensor [10]. This study concluded that a tri-axis reference signal along with 16 order filter NLMS filter with a convergence factor of 0.005 improved the mean square error (MSE) in calculating HR and SpO_2 by 55-60% and 35%-42% respectively, when compared to the existing sensor algorithm which relied solely on moving average filters.

Despite obvious benefits indicated in this study which corroborated the use of ANC filters, there were still some key factors that need to be addressed:

i. The PPG signals were recorded under an experimental protocol which consisted of a single transition from the rest to motion and again went back to rest. Therefore, the true adaptability of these filters when several activities are performed in tandem during a single experiment still needs to be analyzed.

ii. Another potential limitation included the repetitive nature of the noise. For e.g.: Running on a treadmill at a constant pace gave the ANC filters ample time to adapt to the noise. However, the effectiveness of these filters under conditions mimicking practical scenarios with random noise stills needs to be investigated.

iii. Lastly, the suggested method for triggering ANC needs to be examined further. These algorithms triggered ANC filters when the energy of the reference signal exceeded a predefined threshold, which signified excessive movement. This approach has a potential pitfall of not taking into account the nature of the PPG signal which might still be relatively clean despite movement from the subject.

Therefore, to address some of these concerns, we proposed the use ANC filters in combination with K that would serve as precursors for classifying the R/T PPG signals while ANC is used to filter the corrupted segments which are then used for HR sand SpO_2. As a proof of concept, we only used a single ANC filter i.e. NLMS 16^{th} order filter with a convergence factor of 0.01 designed by [10].

10.1. Final Flowchart

The final MNAC flowchart is shown in Figure 10.1 and follows the exact same procedure for processing HR and SpO_2 values as described in section 9.2.2. The only difference here is the use of ANC filters instead of ASAD.

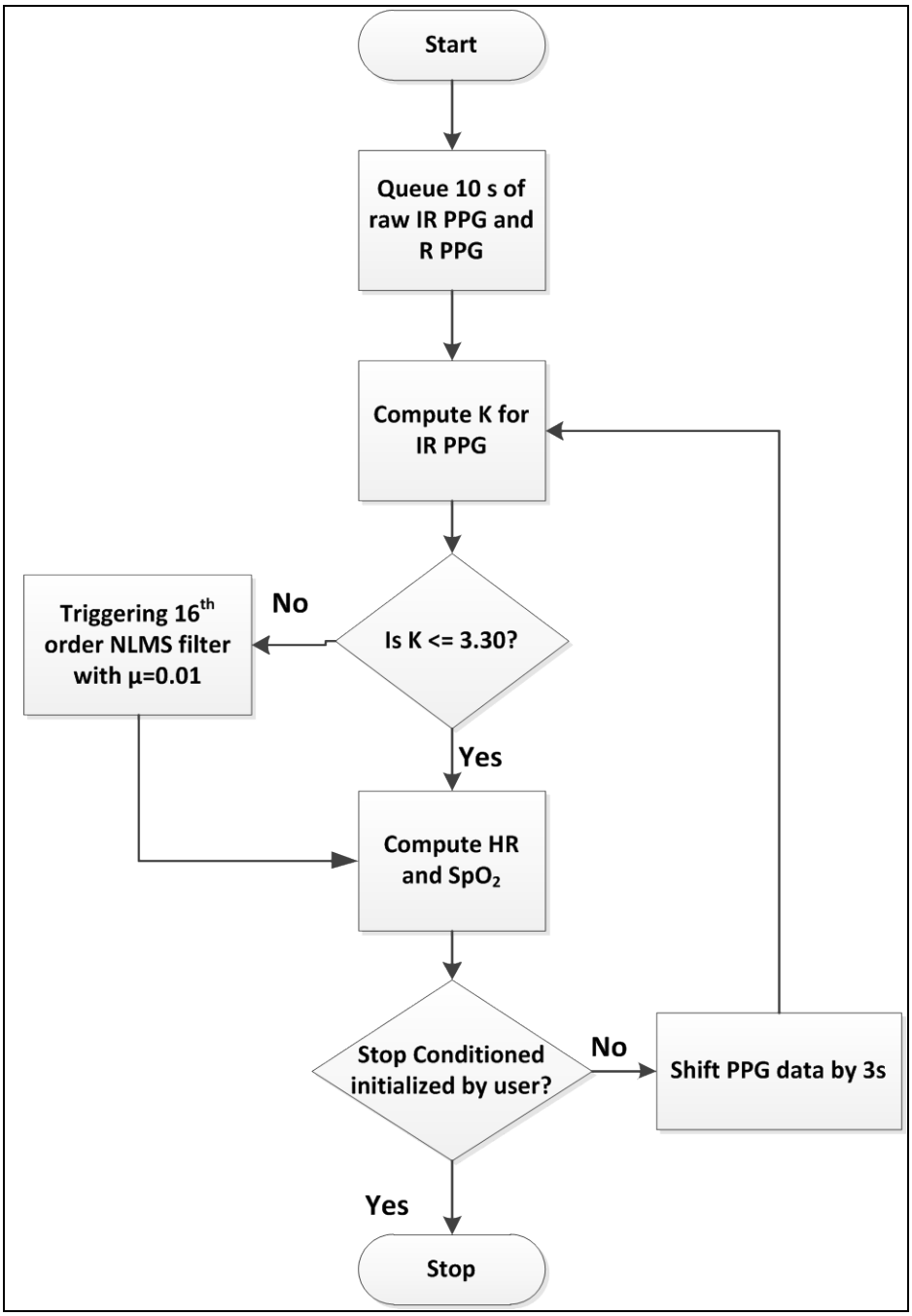

Figure 10.1. Final MNAC algorithm flowchart.

10.2. Timing Diagram

In order to get a clearer perspective on the output frequencies of the novel MA algorithms in comparison to the existing ABS sensor algorithm and the Masimo and CMS 50F pulse oximeters, we constructed a timing diagram shown in Figure 10.2. Here, time is represented by a rectangular wave and the positive peak represents 1 s. For the Masimo and CMS- 50F, we observed that it takes approximately 5 s to output their first HR and SpO_2 values after the sensor is placed on the skin while these devices update these readings every second. The current algorithm represents the embedded algorithm in the ABS sensor takes 15 s to output its first readings and updates them every 0.5 s. Our newly designed algorithms on the other hand would take 10 s to output their first value and update them every 3 s.

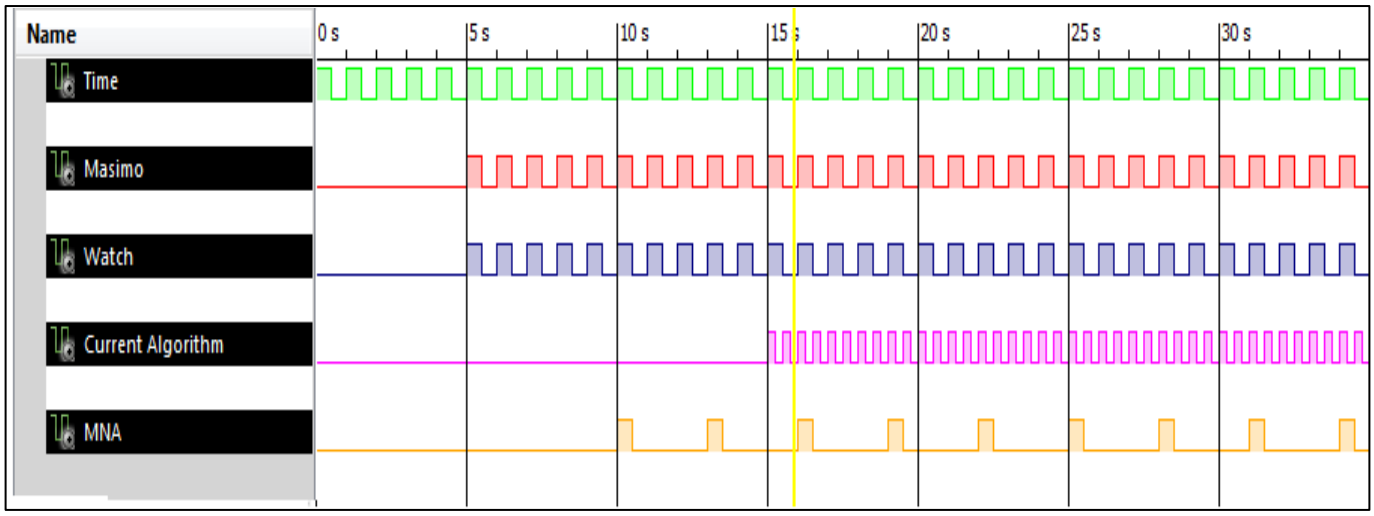

Figure 10.2. Timing Diagram for the novel MA algorithms versus commercial devices.

11. Real Time MNA Implementation

With the design of the final MNA algorithm, a new Labview Virtual Instrument (VI) was developed to implement the MNA algorithm for R/T computation of K, HR and SpO_2. These computed values are time stamped and are stored simultaneously in a text file. This VI is executed with the help of a Mathwork's runtime environment which enables the entire algorithm to be implemented using an equivalent Matlab script. The front panel of the VI as shown in Figure 11.1 is divided into three parts and its features are:

- **A**: Used to turn the software ON/OFF and assign the respective COM-PORT of the computer. The Status LED indicator is used to affirm the constant connection between the sensor and the computer. While the STOP button is to halt the execution of the program.
- **MNA Output (B):** Displays the final values obtained from the MNA algorithm.
- **Saved File Location (C):** The final values are also stored simultaneously in a text file, whose name and memory location can be specified in the "*Filed Path for Saved Data Column*".
- **Sensor Parameters (D):** Used to display the numerical values of the R/T IR and R received directly from the photodetector of the ABS Sensor.

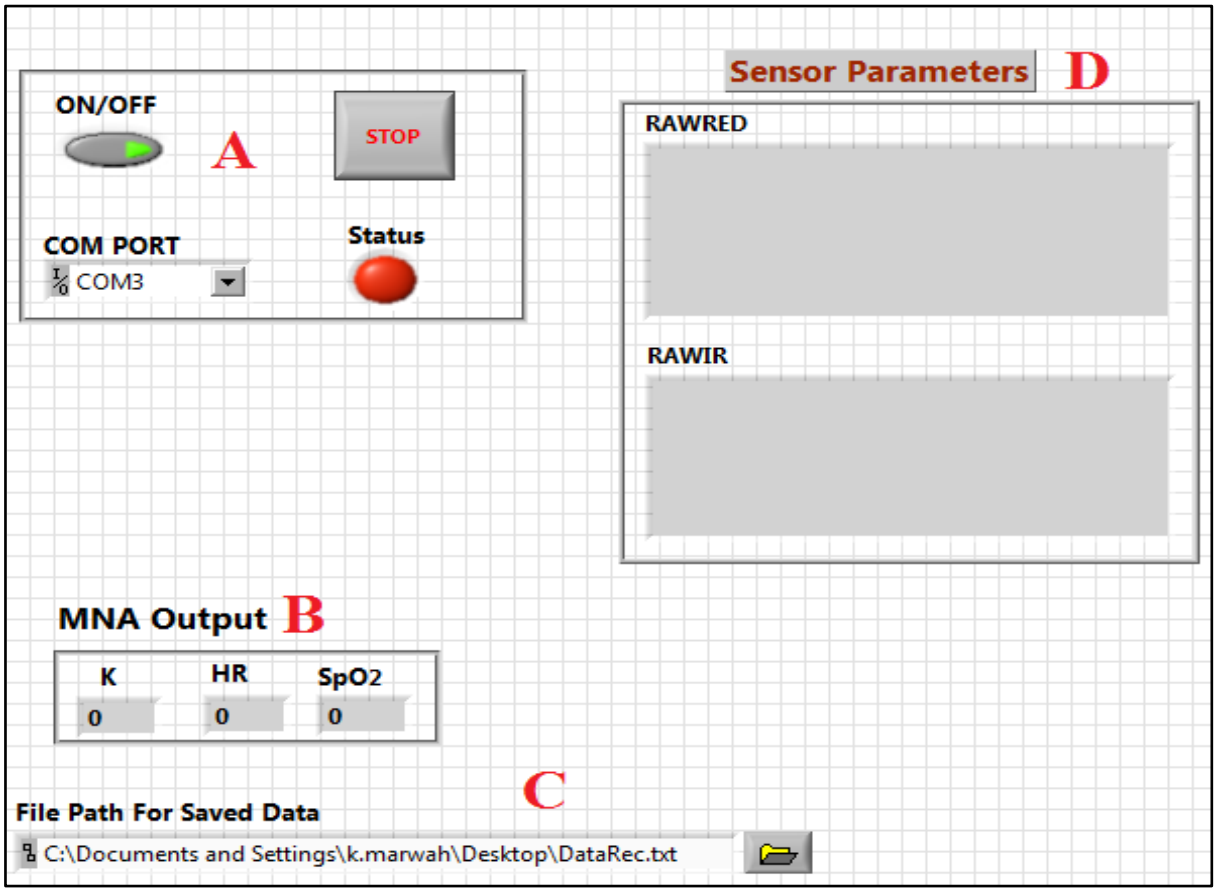

Figure 11.1. Front panel of the VI displaying numerical outputs.

We are also able to graphically plot the raw IR and R PPG's as shown in Figure 11.2 along with the processed MNA algorithm HR and SpO_2 values seen in Figure 11.3.

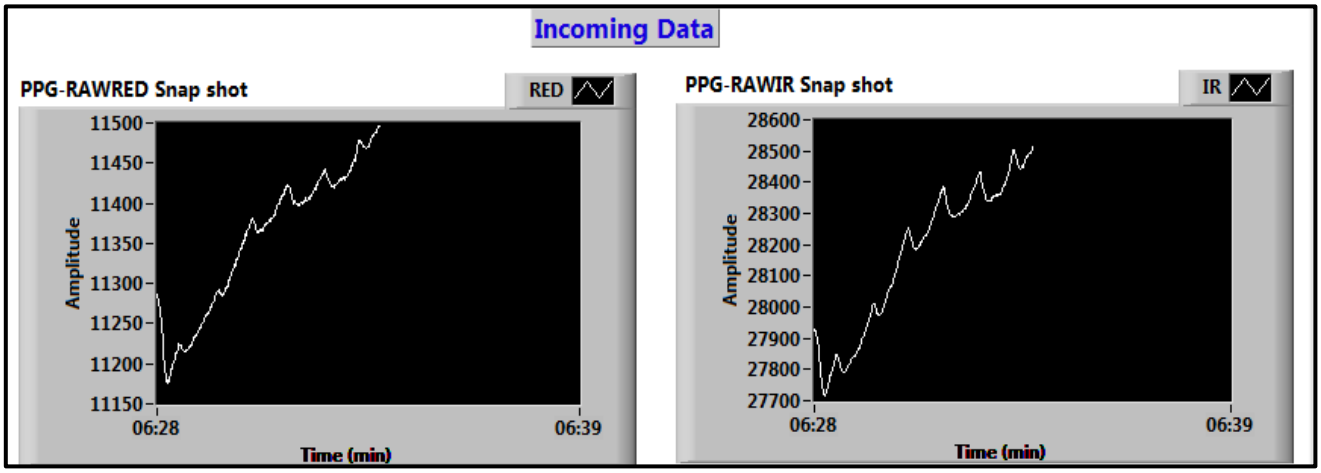

Figure 11.2. R/T plots of raw R and IR PPG.

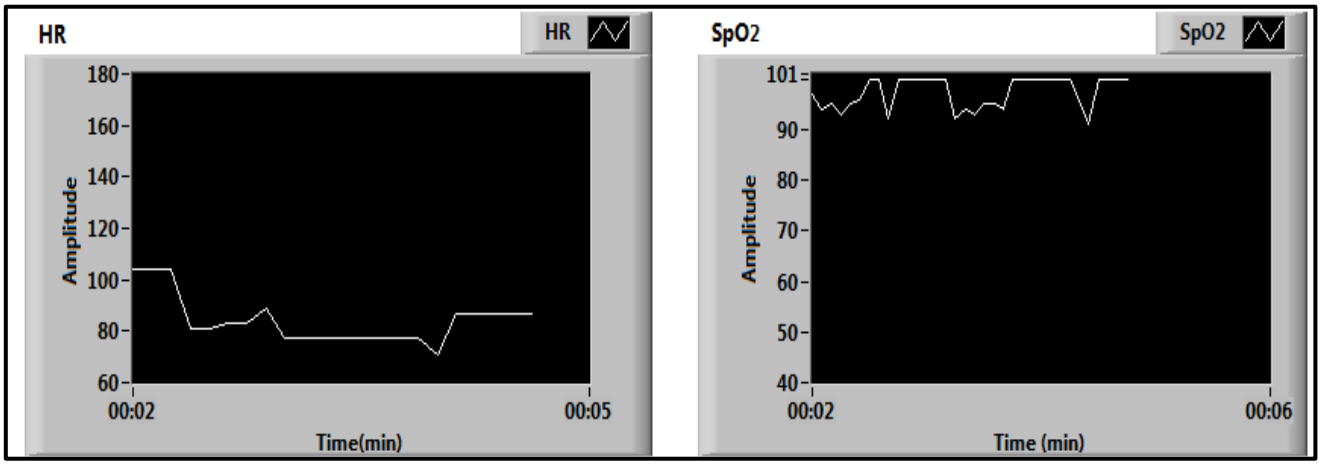

Figure 11.3. Graphical outputs obtained from the MNA algorithm.

As mentioned earlier, these outputs are stored in the form of a text file as shown in Table 11.1. These time stamped vital parameter readings are updated every 3 s and these records can be then further used for medical documentation.

Table 11.1. Sample output obtained from the VI

Date	Time	K	SpO2	HR
2/28/2012	11:54:36 AM	2.21	96.00	53
2/28/2012	11:54:39 AM	2.14	96.00	54
2/28/2012	11:54:42 AM	2.17	96.00	54
2/28/2012	11:54:45 AM	2.30	96.00	54
2/28/2012	11:54:48 AM	2.29	96.00	53
2/28/2012	11:54:51 AM	2.21	96.00	52
2/28/2012	11:54:54 AM	2.20	96.00	52
2/28/2012	11:54:57 AM	2.07	96.00	51
2/28/2012	11:55:00 AM	2.19	96.00	51
2/28/2012	11:55:03 AM	2.09	96.00	51
2/28/2012	11:55:06 AM	2.19	96.00	51
2/28/2012	11:55:09 AM	2.19	96.00	50
2/28/2012	11:55:12 AM	2.22	96.00	50
2/28/2012	11:55:15 AM	2.21	96.00	50
2/28/2012	11:55:18 AM	2.25	96.00	50
2/28/2012	11:55:21 AM	2.25	96.00	50
2/28/2012	11:55:24 AM	2.27	96.00	51
2/28/2012	11:55:27 AM	2.27	96.00	51
2/28/2012	11:55:30 AM	2.10	96.00	51
2/28/2012	11:55:33 AM	2.21	96.00	51
2/28/2012	11:55:36 AM	2.12	96.00	52

12. Discussions

Our goal was to design MA algorithms capable aimed at R/T implementation and capable of being implemented on inexpensive sensor hardware. Here we use a conjunction of technique discussed in chapter 3.2 relating to overcoming MA. Firstly, the MNA algorithm works in conjunction with two principles described earlier; high order statistical tool K [55] and moving average filters [36]. K is responsible for classifying the PPG signals whereas the moving average filters prevent abrupt changes in final HR and SpO_2 readings.

On the other hand, the MNAC works at a preliminary design stage for triggering ANC filters when the computed K is above the designated threshold. This can help in avoiding the ANC filtering of clean PPG which otherwise may cause aberrant vital parameter readings.

These algorithms should be tested during practical application which would induce random noise and help test the ruggedness of these algorithms.

13. Summary and Future Recommendation

13.1. Final Fields Tests for the MNA Algorithms

To assess the functionality of both the MNA/ MNAC algorithms, the next step would be to, conduct field tests to assess the accuracy of HR and SpO_2 while a pool of healthy subjects perform certain daily activities such as stair climbing, brisk walking even jogging.

13.2. Real Time Implementation

Once the functionality of both these algorithms has been analyzed, they can then be embedded in the microprocessor of the ABS sensor and used for all future data classification. Then further tests relating to the power consumption and memory allocation regarding these algorithms can then conducted.

13.3. ANC Filters

As a proof of concept, the MNAC algorithm used the only NLMS adaptive filter that had previously shown to be effective in tackling MA [10]. However, other type of ANC filters, such time varying LMS (TV-LMS) and RLS filters, can also be implemented and tested on the MNAC algorithm. Furthermore, reducing the filter order with difference convergence factors can also be investigated.

13.4. Time Frequency Spectral Analysis

An alternative approach based on time frequency spectral analysis in the HR frequency band can also be investigated for processing corrupted PPG data segments and extracting the HR [55].

14. References

[1] Y. Mendelson, P. Ramuka G. Comtois, "A Comparative Evaluation of Adaptive Noise Cancellation Algorithms for Minimizing Motion Artifacts in a Forehead-Mounted Wearable Pulse Oximeter," in *Engineering in Medicine and Biology Society, 2007. EMBS 2007. 29th Annual International Conference of the IEEE*, Lyons, 2007, pp. 1528-1531.

[2] "Wearable Sports and Fitness Device will hit 90 million shipments in 2017," ABI Research: Technology Market Intelligence, London, 2012.

[3] Kamlin CO, Morley CJ, O'Donnell CP, Donath S, Davis PG. Sekhon JSK, Accuracy of pulse oximetry in assessing heart rate of infants in the neonatal intensive care unit.

[4] Y. Mendelson W. Johnston, "Extracting Heart Rate Variability From A Wearable Reflectance Pulse Oximeter," , 2005.

[5] Y. Shimada and K. Tanaka I. Yoshiya, "Spectrophotometric monitoring of arterial oxygen saturation in the fingertip," *Med. & Biol. Eng: & Comput*, no. 18, pp. 27-32, 1980.

[6] R.J. Duckworth and G.Comtois Y. Mendelson, "A Wearable Reflectance Pulse Oximeter for Remote Physiological Monitoring," in *Engineering in Medicine and Biology Society.28th Annual International Conference of the IEEE*, New York, 2006, pp. 912-915.

[7] W. T. Peruzzi, and R. Templin B. A. Shapiro, *Clinical Application of Blood Gases, 5th ed.* St. Louis, 1994.

[8] JW.Severinghaus and Y. Honda, "History of blood gas analysis. VII. Pulse oximetry," *Journal of Clinical Monitoring and Computing*, vol. 3, no. 2, pp. 135-138, April 1987.

[9] J Allen, "Photoplethysmography and its application in clinical physiological measurement," 2007.

[10] P. Ramuka. (2008, December) Real Time Adaptive Noise Cancellation in Pulse Oximetry: Accurarcy, Processing Speed and Program Memory Considerations. MS Thesis.

[11] P. C. Branche, C. J. Pujary and Y. Mendelson W. S. Johnston, "Effects of motion artifacts on helmet-mounted pulse oximeter sensors," in *Bioengineering Conference, 2004. Proceedings of the IEEE 30th Annual Northeast*, 2004, pp. 214-215.

[12] A. Nagre Y.Mendelson, "Effects of motion artifacts on pulse oximeter readings from different facial regions," in *Bioengineering Conference, 2005. Proceedings of the IEEE 31st Annual Northeast*, 2005, pp. 220-222.

[13] Y. Mendelson, "Pulse Oximetry: Theory and Applicationsfor Noninvasive Monitoring," *Clinical Chemistry*, vol. 38, no. 9, pp. 1601-1607, 1992.

[14] Advance Medical and Health Products. [Online]. http://oximeter.holisticphysio.com/indexE.html

[15] Y. Mendelson and B. D. Ochs, "Noninvasive Pulse Oximetry Utilizing Skin Reflectance Photoplethysmography," *Biomedical Engineering, IEEE Transactions on*, vol. 35, no. 10, pp. 798-805, October 1988.

[16] K. V Madhav, E. H Krishna, K.N Reddy, K.A Reddy M. R. Ram, "On the Performance of Time Varying Step-size Least Mean Squares(TVS-LMS) Adaptive Filter for MA Reduction from PPG Signals," , 2011.

[17] O. Wieben, "Light absorbance in pulse oximetry," in *Design of pulse oximeter*, G. Webster, Ed.

USA: IOP publishing Ltd, 1997, pp. 40-55.

[18] M. Kishi, K. Yamaguchi, and S. Watanabe T. Aoyagi, "Improvement ofan ear-piece oximeter," in *13th Annu. Japanese Soc. Med.*, Osaka, 1974, pp. 90-91.

[19] S.L. Schutz, "Oxygen Saturation Monitoring by Pulse Oximetry," in *AACN Procedure manual for Critical Care*. USA, 2001, ch. 14, pp. 77-83.

[20] S.Holmes and SJ Peffers. (2009, July) General Practice Airways Group: Optimum Respiratory Health. [Online]. http://www.pcrs-uk.org/resources/pulseoximetry_final.pdf

[21] A. R Leyssius and C J. Kalkman, "Influence of Pulse Oximeter Settings On The Frequency Of Alarms And Detection Of Hypoxemia," *JOURNAL OF CLINICAL MONITORING AND COMPUTING*, vol. 14, no. 3, pp. 151-156, 1998.

[22] G Yu, S Santiago, and M Stein A J Williams, "Screening for Sleep Apnea Using Pulse Oximetry and A Clinical Score," *Chest*, vol. 100, no. 3, pp. 613-635, 1991.

[23] T.L. Rusch, J.E. Scharf, and R Sankar, "Alternate pulse oximetry algorithms for SpO2 computation," in *Engineering in Medicine and Biology Society, 1994. Engineering Advances: New Opportunities for Biomedical Engineers.*, 1994, pp. 848-849.

[24] JW. Severinghaus and PE. Bickler JR. Feiner, "Dark skin decreases the accuracy of pulse oximeters at low oxygen saturation: the effects of oximeter probe type and gender," *Anesth Analg*, vol. 6, pp. S18-23, December 2007.

[25] HS Mathewson JM Kim, "Venous congestion affects arterial hemoglobin saturation measured by a pulse oximeter.," *Anesthesiology*, vol. A, no. 174, p. 63, 1985.

[26] G.Mardirossian and R. E. Schneider, "Limitations of Pulse Oximetry," *Anesth Prog*, vol. 39, no. 6, pp. 194-196, 1992.

[27] J.A. Langton and C.D Hanning, "Effect of motion artefact on pulse oximeters: evaluation of four instruments and finger probes," *British Journal Of Anaesthesia*, vol. 65, no. 4, pp. 564-570, 1990.

[28] N.K. Shah. S. J. Barker, "The Effects of Motion on the Performance of Pulse Oximeters in Volunteers," *Anesthesiology*, vol. 86, pp. 101-108, 1996.

[29] V. L. Begnoche and J. M. Graybeal M. T. Petterson, "The Effect of Motion on Pulse Oximetry and Its Clinical Significance," *Anesthersia & Analgesia*, vol. 105, no. 65, pp. S78-S84, December 2006.

[30] S. Lawless, "Crying wolf: false alarms in a pediatric intensive care unit," *Crit Care Med*, vol. 22:, pp. 981–5, 1994.

[31] B. Hok, K. Stahl and A. Jordeby-Jonsson L. Wiklund, "Postanesthesia monitoring revisited: frequency of true and false alarms from different monitoring devices," *J Clin Anesth*, vol. 6, pp. 182-8, 1994.

[32] Southeastern Medical Supply. [Online]. http://www.semedicalsupply.com/CMS50F-Wrist-Sleep-Study-Pulse-Oximeter-with-Alarm-p/cms50fw.htm

[33] P. I. Reynolds, T.VLewis, M. Siewert, D. Watson, A. R. Tait and K.Tremper, S. Malviya, "False Alarms and Sensitivity of Conventional Pulse Oximetry Versus the Masimo SET™ Technology in the Pediatric," *Anesth Analg*, vol. 90, pp. 1336 –40, June 2000.

[34] A. Dixon. (2011, May) Livestrong.com. [Online]. http://www.livestrong.com/article/278796-oxygen-saturation-exercise/

[35] G. Zeman and B. Make, "Clinical Window to Real-world Oximetry Exercise Testing.," *Anaesthesiology*, pp. 50-67, 2005.

[36] J.W Lee, W.G Jung and G.K Lee H. W. Lee, "The Periodic Moving Average Filter for Removing Motion Artifacts from PPG Signals," *Journal of Control, Automation, and Systems*, vol. 5, no. 6, pp. 701-706, December 2007.

[37] B.S. Kim and S. Sun, "Motion Artifact Reduction in Photoplethysmography Using Independent Component Analysis," vol. 53, no. 3, 2006.

[38] A. Reddy and V. Jagadeesh K. Kumar, "Motion Artifact Reduction in Photoplethysmographic Signals using Singular Value Decomposition," in *Instrumentation and Measurement Technology Conference Proceedings, 2007. IMTC 2007. IEEE*, Warsaw, Poland, 2007, pp. 1-4.

[39] C. M. Lee and Y. T. Zhang, "Reduction of Motion Artifacts from Photoplethysmographic Recordings Using a Wavelet Denoising Approach," vol. 3, 2003.

[40] JYA. Foo., "Comparison of wavelet transformation and adaptive filtering in restoring artefact-induced time-related measurement," *Biomedical Signal Processing and Control*, no. 1, pp. 93-98, January 2006.

[41] M. Bawa, M. Tahernezhadi. KVP. Naraharisetti, "Comparison of Different Signal Processing Methods for Reducing Artifacts from Photoplethysmograph Signal," in *Electro/Information Technology (EIT), 2011 IEEE International Conference on*, 2011, pp. 1-7.

[42] J. Y. Warren and S. Warren, "A short study to assess the potential of independent component analysis for motion artifact separation in wearable pulse oximeter signals," , Shanghai, 2005.

[43] L. M. Vicente, I. K. Persad A. B. Barreto, "Adaptive Cancelation of Motion Artifact in Photoplethysmographic Blood Volume Pulse Measurements for Exercise Evaluation," , 1995.

[44] M.A.D. Raya and L.G. Sison, "Adaptive Noise Cancelling of Motion Artifact in Stress ECG Signals Using Accelerometer," in *Engineering in Medicine and Biology, 2002. 24th Annual Conference and the Annual Fall Meeting of the Biomedical Engineering Society EMBS/BMES Conference, 2002. Proceedings of the Second Joint*, Houston, 2002, pp. 1756-1757.

[45] J. R. J. Glover, J. M. McCool, J. Kaunitz, C. S. Williams, R. H. Hearn, J. R.Zeidler, E. Dong and R. C. Goodlin B. Widrow, "Adaptive noise cancelling: Principles and applications," vol. 63, no. 12, 1975.

[46] N. C. Swenson, and R. W. Picard M.Z. Poh, "Motion Tolerant Magnetic Earring Sensor and Wireless Earpiece for Wearable Photoplethysmography," *IEEE Transactions On Information Technology In Biomedicine*, vol. 14, no. 3, pp. 786-794, May 2010.

[47] M.J Kim, and J. Kim H. Han, "Development of real-time motion artifact reduction algorithm for a wearable photoplethysmography," in *Proceedings of the 29th Annual International Conference of the IEEE EMBS*, Lyon, France, 2007, pp. 1538-1541.

[48] K.V. Madhav, E. H Krishna, K.A. Reddy and K.N Reddy M.K. Ram, "On the performance of AS-LMS based Adaptive Filter for Reduction of Motion Artifacts from PPG Signals," , 2011.

[49] M. R. Homaeinezhad, M. Khazraee and M. M. Daevaeiha A. Ghaffari, "Segmentation of Holter ECG Waves Via Analysis of a Discrete Wavelet-Derived Multiple Skewness–Kurtosis Based Metric," vol. 38, 2010.

[50] T. Sejnowski and S. Makeigb A. Delorme, "Enhanced detection of artifacts in EEG data using higher-order statistics and independent component analysis," *NeuroImage*, vol. 34, pp. 1443-1449, November 2006.

[51] B. Natarajan and S. Warren R. Krishnan, "Two-Stage Approach for Detection and Reduction of Motion Artifacts in Photoplethysmographic Data," *Biomedical Engineering, IEEE Transactions* , vol. 57, no. 8, pp. 1867- 1876 , August 2010.

[52] S. Haykin and B. Widrow, *Least-Mean-Square Adaptive Filters*. USA: Wiley, 2003.

[53] G. Comtois, Adaptive Noise Cancellation Utilizing Accelerometer to Reduce the Effects of Motion Artifact in Wearable Reflectance Mode Pulse Oximetry, 2007, M.S. Thesis, Department of Biomedical Engineering, Worcester Polytechnic Institute, Worcester, MA.

[54] Z. M. Hussian and R. Harris Y. S. Lau, "Performance of Adaptive Filtering Algorithms: A Comparative Study," in *Australian Telecommunications, Networks and Applications Conference (ATNAC)*, Melbourne, 2003.

[55] Y. Mendelson, K. H. Shelley, D. G. Silverman and K. H. Chon* N. Selvaraj, "Statistical approach for the detection of motion/noise artifacts in Photoplethysmogram," in *Annual International Conference of the IEEE Engineering in Medicine and Biology Society. IEEE Engineering in Medicine and Biology Society. Conference*, Boston, 2011, pp. 4972-5.

[56] Zhang Yi. Zhi-Lin Zhang, "Extraction of a source signal whose kurtosis values lie in a specific range,".

[57] J.McNames, T.Thong, D.Tsunami, M.S Ellenby, B.Goldstein M. Aboy, "An Automatic Beat Detection Algorithm for Pressure Signals," *IEEE Trans. Biomed. Eng.*, vol. 52, no. 10, pp. 1662-1670, October 2005.